A CaSSIS and HiRISE map of the Clay-bearing Unit at the ExoMars 2022 landing site in Oxia Planum

Adam Parkes Bowen [a,*], John Bridges [a], Livio Tornabene [b], Lucia Mandon [c], Cathy Quantin-Nataf [d], Manish R. Patel [e], Nicolas Thomas [f], Gabriele Cremonese [g], Giovanni Munaretto [g,h], Antoine Pommerol [f], Maurizio Pajola [g]

[a] Space Park Leicester, School of Physics and Astronomy, University of Leicester, LE1 7RH, UK
[b] Institute for Space & Earth Exploration, Department of Earth Sciences, Western University, 1151 Richmond St, ON, N6A 3K7, Canada
[c] LESIA, Observatoire de Paris, Université PSL, CNRS, Sorbonne Université, Université de Paris, 5 Place Janssen, 92195, Meudon, France
[d] Université Claude Bernard Lyon 1, 43 Boulevard du 11 Novembre 1918, 69100, Villeurbanne, France
[e] School of Physical Sciences, The Open University, Walton Hall, Milton Keynes, MK7 6AA, UK
[f] Physikalisches Institut, Universität Bern, Hochschulstrasse 6, 3012, Bern, Switzerland
[g] INAF-Astronomical Observatory of Padova, Vicolo dell'Osservatorio, 5, 35122, Padova, PD, Italy
[h] University of Padova, Department of Physics and Astronomy, Padova, Italy

ARTICLE INFO

ABSTRACT

In preparation for the operations of the ExoMars Rosalind Franklin rover, characterising its landing site in Oxia Planum is essential. Of particular interest is the extensive Clay-bearing Unit present at the site, a key target in the search for biosignatures. In this paper we provide a map based on variations in colour and spectral information within this unit, covering the 1σ landing envelope of the rover along with a 1 km buffer to account for minor shifts of the landing envelope ahead of launch (referred to going forward as the 1σ+ landing envelope). We used imagery from the Colour and Stereo Surface Imaging System (CaSSIS) and High Resolution Imaging Science Experiment (HiRISE) instruments, along with CaSSIS Band Ratio Composites with enhanced colour sensitivity to the presence of ferric (Fe^{3+}) and ferrous (Fe^{2+}) iron bearing materials. Our map is of a far higher resolution (map-scale 1:2000) than those previously available and, in contrast to previously available maps of this unit, differentiates between an Orange Subunit and a Blue Subunit which make up the Clay-bearing Unit. This mapping covered the ~91% of the 1σ+ landing envelope where there was CaSSIS coverage and split the Clay-bearing Unit into three categories: one for each of the clay subunits, and another for exposures of the Clay-bearing Unit where either both subunits were too intermixed to reliably separate, or where it was difficult to determine which of the two were present.

The results from our mapping shows that at least ~35% of the 1σ+ envelope is covered by exposures of the Clay-bearing Unit: ~18% by the Orange Subunit, ~9% the Blue Subunit, and ~12% were classified as Indeterminate. The spread of these two subunits varied substantially over the 1σ+ landing envelope, with the south-east half of the landing envelope dominated by the Orange Subunit (~70% exposures in this area belonging to the Orange Subunit, ~10% to the Blue Subunit and ~20% to the Indeterminate category), while the north-west has more sporadic exposures of the Clay-bearing Unit (~22% Orange, ~37% Blue and ~41% Indeterminate). The colour distinction between the two subunits is thought to be due to constituent mineralogical differences rather than differences in dust coverage of the two subunits. The scale of the fracturing present in the two subunits has also been assessed in this study, via qualitative observations of the fracture length and quantitative mapping out of fracture networks. While there were differences in the scale of fracturing between the two subunits, these were not as great as had previously been identified.

1. Introduction

The ExoMars Rosalind Franklin rover is due to begin investigations of the Martian surface in summer 2023, with the goals of searching for signs of past and present life on Mars along with investigating the water content and geochemical variations in the subsurface (Vago et al. 2015, 2017). To achieve these goals, characterisation of the landing site ahead of the arrival of the rover is essential for interpreting the geology of the site, planning prospective traverses, and future selection of drill sites (Vago et al., 2015; Pajola et al., 2017; Mastropietro et al., 2020).

The landing site is located within the plains of Oxia Planum, between 17 to 19° North and 335 to 336.5° East, at the outlet of the Coogoon Valles system (Molina et al., 2017), a valley network situated at the margin between the uplands of Arabia Terra and lowlands of Chryse Planitia (Tanaka et al., 2014). Oxia Planum was chosen for the ExoMars2022 mission as it once hosted a sustained, long-lived aqueous environment, as evidenced by the presence of a widespread, Noachian-aged layered Fe/Mg clay-bearing deposit which appears to drape the pre-existing topography (Quantin-Nataf et al. 2015, 2021). Appearing light-toned and extensively fractured, this unit is ~50–100 m thick, with identifiable individual layers ~0.7–3 m thick. Spectral datasets available of the Clay-bearing Unit indicate that the Fe/Mg clay present is most likely a Fe/Mg-rich saponite or vermiculite (Carter et al., 2016). Both are Fe/Mg phyllosilicates, with saponite being trioctahedral and vermiculite either trioctahedral or dioctahedral.

Several landforms present at the site suggest that subsequent episodes of aqueous activity occurred at Oxia Planum after the formation of the Clay-bearing Unit. These landforms include deltaic deposits, which are thought to have formed within a standing body of liquid water during the Noachian, and a series of channels incised into the Clay-bearing Unit which are thought to have formed after the water level dropped (Molina et al., 2017; Quantin-Nataf et al., 2021). The largest examples of these deltaic deposits and channels are highlighted in Fig. 1. Sporadic outcrops of an Al Clay-bearing Unit have also been detected at the landing site,

with the best detections being around the large deltaic deposit in the south-east of the site (Carter et al., 2016; Quantin-Nataf et al., 2017). As these outcrops have no noted relation to the other units and features present at Oxia Planum, potential formation mechanisms are currently unknown (Carter et al., 2016).

Two units which are comprised of unaltered materials are also present. One of these, the Dark Resistant Unit (DRU), consists of several large exposures across the landing site (total area of those shown in Fig. 1 being ~740 km^2) and originated either in the early Hesperian (Gary-Bicas and Rogers, 2021) or in the early Amazonian (Quantin-Nataf et al., 2021). Another, the smooth Dark Mantling Unit (DMU, example
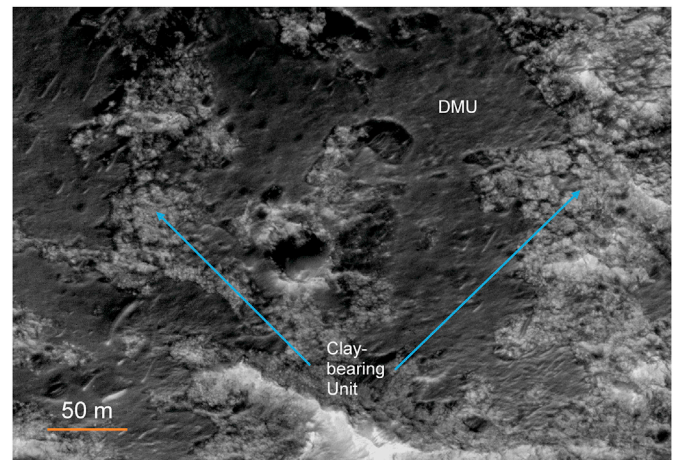

Fig. 2. An example of the DMU i.e. the smooth, dark material, can be seen here overlying sections of the Clay-bearing Unit, which appears bright and fractured. The HiRISE image ID is [ESP_42701_1980]. See Fig. 3 for the locations of this site within Oxia Planum.
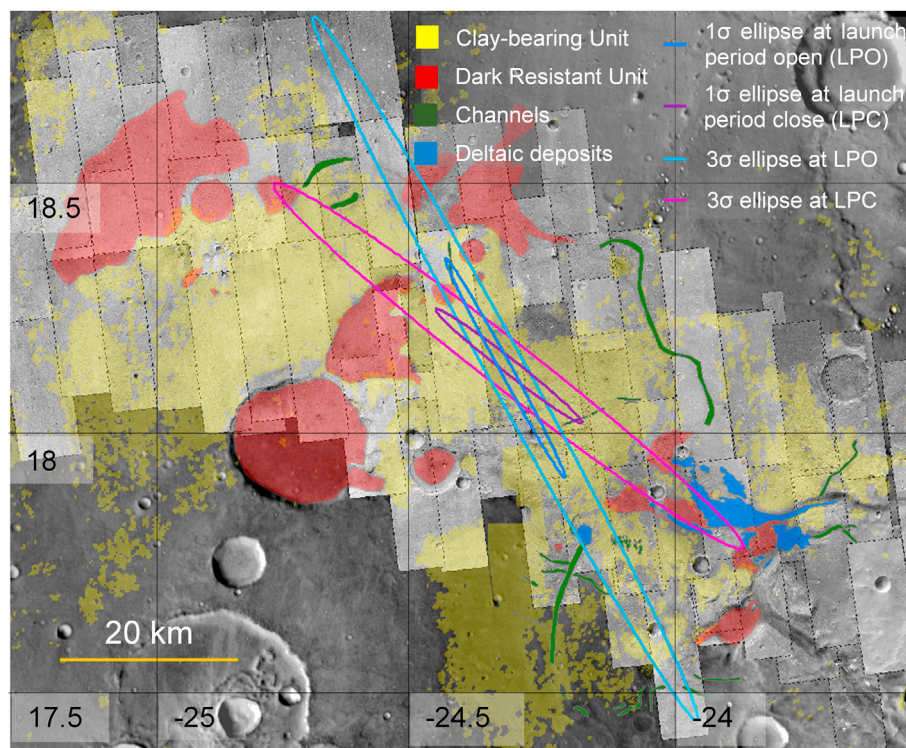

Fig. 1. HiRISE images available of Oxia Planum as of the 20th December 2020, this being overlaid on a normalised THEMIS daytime IR brightness temperature mosaic (Fergason, 2014). This shows the extent of the Dark Resistant Unit, deltaic deposits, channels and clay-bearing deposits. The map of the Clay-bearing Unit is from Carter et al. (2016) while the extent of the Dark Resistant Unit, delta and fluvial units shown are recreated from Quantin-Nataf et al. (2021).

shown in Fig. 2), consists of large deposits located north-west of the fan-like deltaic deposit (see Fig. 15 in (Quantin-Nataf et al., 2021)), along with smaller exposures elsewhere at the site which often appear as inverted crater fills in the sites decametre-sized craters (Quantin-Nataf et al., 2021). It is not possible to show a comprehensive map of this unit as mapping of it is still ongoing.

1.1. Prior investigations of the Clay-bearing Unit

Several hypotheses have been put forward to explain the formation mechanism of the Clay-bearing Unit and the origin of the constituent clay minerals (Mandon et al., 2021; Quantin-Nataf et al., 2021). It has been suggested that the clays could have formed in situ, during or after deposition of what is now the Clay-bearing Unit, or be detrital, being derived from the large catchment area of Oxia Planum (Fawdon et al., 2019; Quantin-Nataf et al., 2021). If formed in situ, sedimentary deposition in a palustrine, lacustrine, or marine setting are possibilities (Carter et al., 2016), as are volcaniclastic sediments altered by meteoritic water. Other mechanisms, such as that of a thinly layered lava flow stack which experienced post-emplacement alteration into clays, are also possible (Quantin-Nataf et al., 2021). If the clay minerals are detrital in origin the previously mentioned mechanisms could be responsible for the clay minerals formation elsewhere within the site's extensive watershed prior to being delivered to Oxia Planum (Fawdon et al., 2019). In addition to these, impact-altered minerals originating from the heavily cratered Noachian crust of Arabia Terra (Tornabene et al., 2013) within this watershed could be the source of the clay minerals at the site.

Initially when Oxia Planum was being assessed as a landing site candidate, the Clay-bearing Unit was mapped out across the engineering envelope of the landing site, this being the area analysed at a macro scale in order to decide on the exact placement of the rover landing envelope. This was done using the OMEGA (Observatoire pour la Minéralogie, l'Eau, les Glaces et l'Activités) and CRISM (Compact Reconnaissance Imaging Spectrometer for Mars) instruments, with the resulting map shown in Fig. 1 (Carter et al., 2016). These instruments are hyperspectral spectrometers: OMEGA images in the 0.38–5.1 μm spectral range across 352 channels (Bibring et al., 2004), while CRISM operates in the 0.36–3.92 μm spectral range. This is done across either 55–154 channels when operating in the scanning mode, this being the mode used in the mapping shown in Carter et al. (2016), or across 545 channels when operating in its hyperspectral mode (Murchie et al., 2007). Data from these instruments have been useful for assessing the mineralogy of the site and aiding the formation of testable hypotheses prior to the arrival of the rover. However the low resolution of the data from these instruments,

with OMEGA data at best being ~350 m but often >1 km/pixel and CRISM data being 100–200 m/pixel when operating in its scanning mode (Bibring et al., 2004; Murchie et al., 2007), precludes use of this map, created as part of an investigation of mineralogical composition, for other purposes.

This prior mapping also does not differentiate between two subunits which were subsequently found to make up the Clay-bearing Unit, this being discovered by Mandon et al. (2021) via co-analysis of HiRISE (McEwen et al., 2007), CaSSIS (Thomas et al., 2017), and 20–40 m/pixel targeted CRISM data (Murchie et al., 2007). One subunit appears orange in HiRISE and CaSSIS visible to near infrared (VNIR) colour images and is observed to be consistently overlain by an upper subunit which appears bluish in the same imagery (Fig. 4). Both subunits were found to be extensively fractured within HiRISE imagery and were reportedly distinguishable according to the scales of fracturing present. The Orange Subunit was found to exhibit extensive fracturing at the metre-scale with decametre-scale fractures also present, while the Blue Subunit was found to possess decametre-scale fracturing (Mandon et al., 2021; Quantin-Nataf et al., 2021). Exposures of these two subunits were also mapped based on the colouration of the Clay-bearing Unit, with this being done using HiRISE colour data. This was undertaken as a point mapping exercise, with exposures of the two subunits being identified where there was HiRISE colour coverage across the engineering envelope (~25% of the total area when this was carried out), with the data summarised using a grid of 1 km^2 cells for clarity (see Fig. 3 in (Mandon et al., 2021)).

Available CRISM targeted data of these subunits revealed that the Orange Subunit has spectral signatures indicating the presence of Fe/Mg-rich phyllosilicates, with the best spectral match being a vermiculite or an Fe-saponite (Carter et al., 2016). The Blue Subunit shows spectral signatures consistent with a mixture between the same clay mineral and olivine, this olivine spectral signature being consistent with that of fayalite or coarse grained forsterite (Mandon et al., 2021). CaSSIS Colour Band Ratio Composites (CBRCs), which are comprised of spectral band ratios designed to distinguish between surface components, in this case ferric and ferrous iron-bearing and non-iron-bearing materials (Tornabene et al., 2018, Tornabene et al. in prep), shows that the Orange Subunit appears to be ferric-bearing and the Blue Subunit more ferrous in comparison. This is consistent with the presence of vermiculite or Fe-saponite within the Orange Subunit, while the more ferrous nature of Blue Subunit exposures is consistent with fayalite or fosterite being present. Furthermore, these areas strongly correlate with those that are Fe/Mg clay-bearing in CRISM targeted data (see Fig. 5).

1.2. Creating a new map of the Clay-bearing Unit

These earlier mapping efforts, while successful in what they were constructed to do i.e. to provide a macroscale map of the Clay-bearing Unit and to identify the broad-scale distribution of the two clay-bearing subunits respectively, are limited in their applications due to the resolution of the former and spatial extent of the latter. It is this which we sought to address here: within this work we use high resolution CaSSIS imagery, supplemented by HiRISE, to identify and map the two clay-bearing subunits via their unique colouration, spectral characteristics, texture (i.e. fracturing) and the stratigraphic relationships between each other (Carter et al., 2016; Quantin-Nataf et al., 2021). This mapping was undertaken at a 1:2000 map scale and was intended to map the exact spatial extent of the subunit exposures present, rather than identify examples of the clay subunit as was done in (Mandon et al., 2021). This mapping effort was limited to the 1σ+ envelope which had CaSSIS coverage, this constituting an area of ~163 km^2, i.e. ~91% of the total 1σ+ envelope. However this is still a substantial improvement over the coverage provided by HiRISE colour imagery, which stands at ~44% as of the writing of the end of 2021.

This effort, in addition to providing a comprehensive map of the two clay-bearing subunits, provides a significantly higher resolution map of the overall Clay-bearing Unit over the 1σ+ envelope than is currently
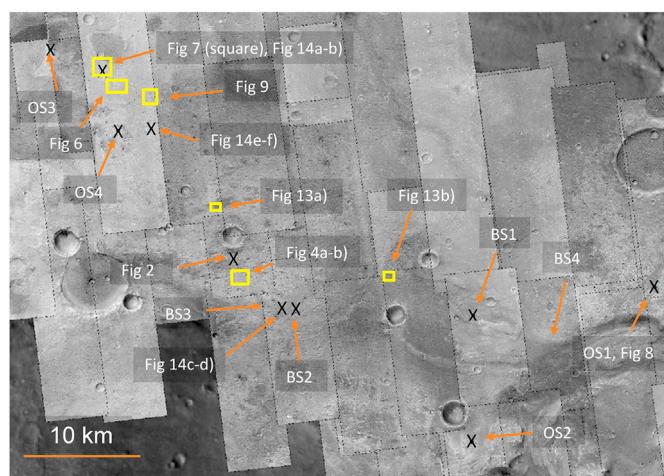

Fig. 3. Location of the various exposures and areas referred to in the text. BS refers to the Blue Subunit, and OS to the Orange Subunit.
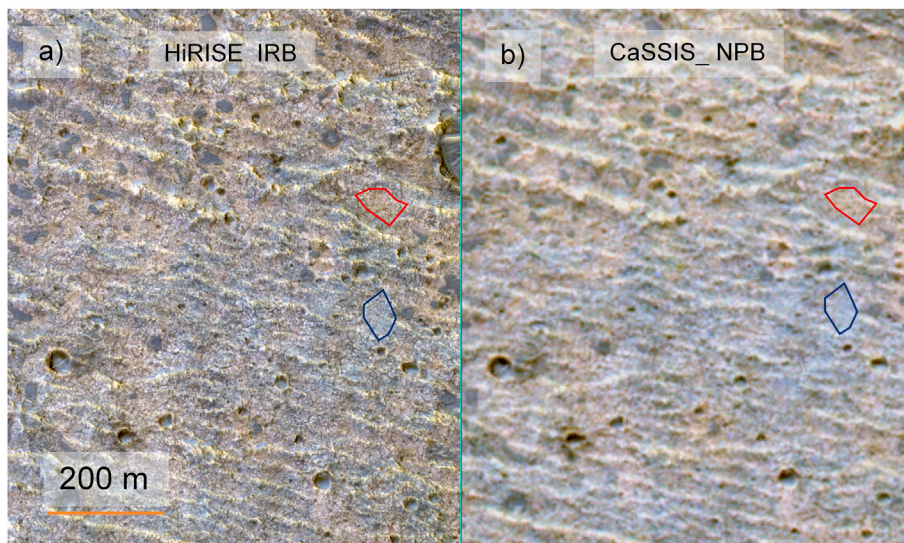
Fig. 4. Examples of the orange lower and blue upper clay-bearing subunits, shown in HiRISE IR-RED-BG [IRB] [a] and CaSSIS NIR-PAN-BLU (NPB) (b). The HiRISE image ID is [ESP_068522_1980] and the CaSSIS image ID is [MY35_009481_165_0]. Examples of the Orange and Blue Subunits are highlighted in red and blue respectively. Note that the stretch used for the CaSSIS image was histogram-matched for each band to the HiRISE colour image. See Fig. 3, which provides additional context for the locations of these sites within Oxia Planum.
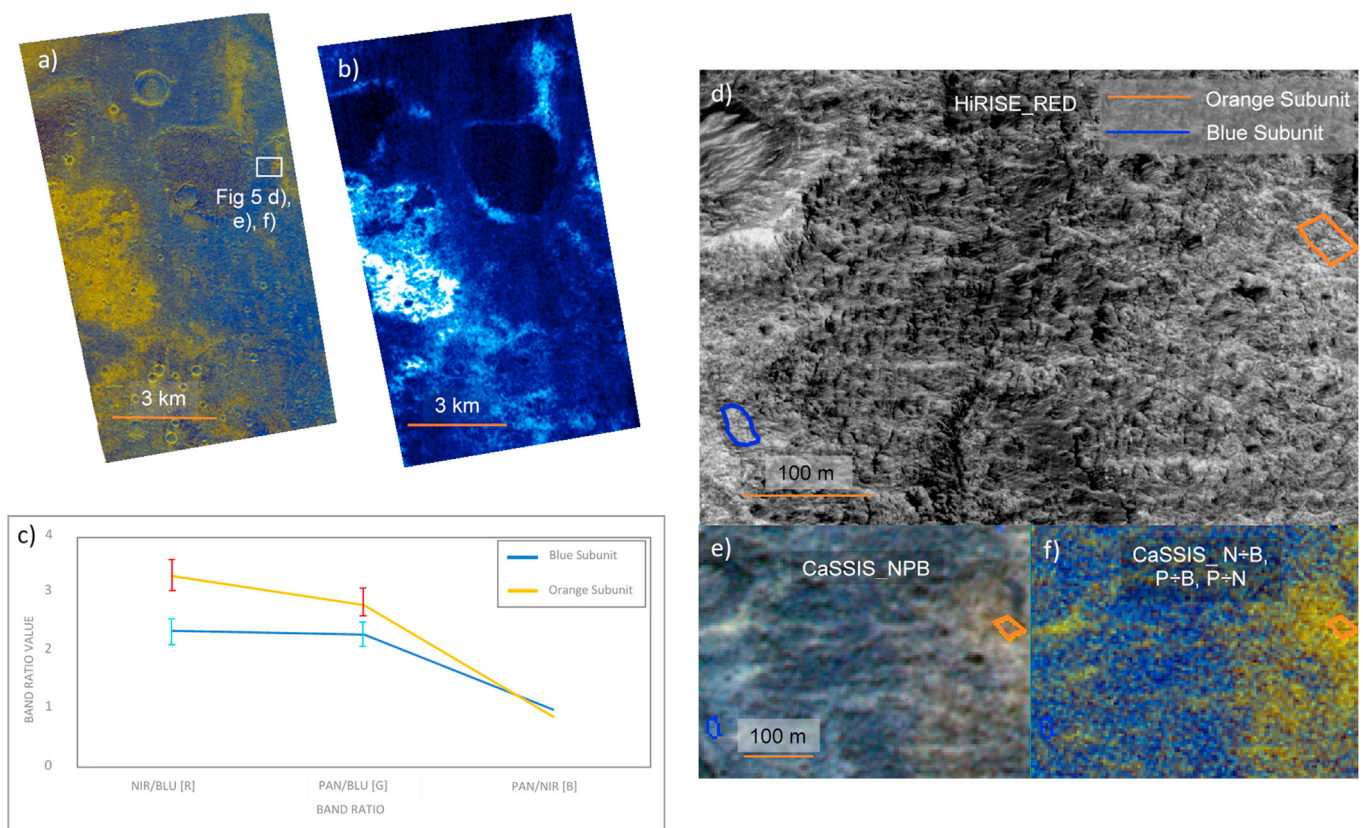

Fig. 5. (a) A CaSSIS Colour Band Ratio Composite (CBRC) "NPBb" product, which is comprised of NIR/BLU, PAN/BLU and PAN/NIR ratios in the R-G-B channels respectively based on CaSSIS image [MY35_008275_165_0]. (b) A CRISM targeted spectral D2300 parameter image. This parameter measures the reflectance drop-off at 2.3 μm (Viviano-Beck et al., 2014), usually consistent with the presence of hydrated/hydroxylated Fe/Mg-rich minerals or carbonates, and is used here to highlight the clay-bearing areas covered by the CRISM image [frt0000810d_07_sr166j_mtr3]. It can be seen that those areas that register as distinctly ferric (yellow) in the CaSSIS CBRC-NPBb product correlate strongly with increased D2300 band strength (cyan) in the CRISM spectral product. (c) Spectral plot showing a comparison between exposures of the Orange and Blue Subunits covering an area of ~385 m^2 and ~300 m^2 respectively (averaged from 24 and 19 pixels respectively). The error bars shown are the standard deviation for each band ratio. These exposures are shown in HiRISE, CaSSIS and CBRC products within Fig. 5 d, e and f) respectively. The HiRISE image ID is [ESP_037558_1985], while the CaSSIS image ID is [MY35_008275_165_0] Mapping of the subunit exposures are overlaid onto each image.

available. This map will have multiple key uses after the arrival of the rover: it will provide context on the Oxia Planum region to the ground-truth investigation carried out by the rover; it will be useful in determining the mechanism via which these subunits formed; and it will aid navigation of the rover to exposures of the two subunits, which are high-priority science targets due to both the high biosignature preservation potential of the clay minerals and what the subunits indicate about the shifting environment at Oxia Planum.

2. Data sets and methods

2.1. Data sets used in this study

Identifying exposures of the Clay-bearing Unit, and distinguishing between the two clay-bearing subunits, were the main challenges in this study. In order to precisely determine the extent of the light-toned, fractured terrain characteristic of the Clay-bearing Unit, HiRISE images were utilised. HiRISE is a VNIR pushbroom imager operating over the wavelength range of 400–1100 nm, this being divided across three filters, or bands, as follows: BG (blue-green; 400–600 nm, band centre (BC); 536 nm), RED (a broad panchromatic band centred on red; 550–850 nm, BC; 694 nm) and NIR (infrared; 800–1100 nm, BC; 874 nm) (McEwen et al., 2007). It possesses the highest resolution of any Mars imager at 0.25 m/pixel for the RED band and 0.5 m/pixel for the BG and IR bands, allowing it to be used to confidently identify objects on the order of 0.5–0.75 m in diameter when using the greyscale HiRISE RED products. While HiRISE possesses the ability to image in colour, the swath of the colour overlap region only extends across 1–1.2 km (~20%) of each 5–6 km wide HiRISE footprint, with this latter footprint consisting of only the RED band. Given the narrow swath width of HiRISE colour images and the impractically high number of such images required to get full mosaicked coverage of the landing site, HiRISE is unsuitable for observing the colouration of the Clay-bearing Unit across the entire study area and consequently cannot be used for creating a contiguous map of the two clay-bearing subunits across the site. HiRISE RED imagery was instead used to determine the presence and extent of Clay-bearing Unit exposures via identifying the light-toned, fractured terrain characteristic of it. This allowed a higher resolution mapping of the two subunits than would otherwise be possible.

Given the limited HiRISE colour coverage, CaSSIS was used to provide colour information for this study. CaSSIS possesses ~91% coverage of the 1σ+ envelope in high resolution at 4.5 m/pixel, which is map-projected and resampled to 4 m/pixel (Perry et al. this issue). CaSSIS is a VNIR pushframe imager which images across a similar wavelength range to HiRISE at ~400–1100 nm across four colour bands as follows; BLU (blue-green; 363–632 nm, BC; 497 nm), PAN (a broad panchromatic band centred on red; 446–909 nm, BC; 677 nm), RED (infrared; 737–933 nm, BC; 835 nm) and NIR (infrared; 820–1061 nm, BC; 940 nm). It is also able to take stereo images within a single pass of a target by rotating independently of the spacecraft (Thomas et al., 2017). CaSSIS NIR-PAN-BLU and RED-PAN-BLU images are nearly identical to HiRISE IR-RED-BG images in terms of the colours observed of the imaged terrain. Due to a data read out bottleneck issue (Pommerol et al. this issue), CaSSIS cannot image with all 4 filters over the full 2048-pixels from the current altitude of the host orbiter ExoMars Trace Gas Orbiter (TGO). Consequently CaSSIS can either image a 7.5 km swath in all four colours or its entire swath width of ~9.5 km using three colours, though this maximum swath width is only achieved over the mid to high northern latitudes. The decision of which imaging mode is utilised is made by the image's planner (Almeida et al. this issue).

Alongside the CaSSIS and HiRISE data sets, a merged HiRISE-CTX DEM, georeferenced to the HRSC MC11W mosaic (Gwinner et al., 2016; Sefton-Nash et al., 2020), was used to assess the stratigraphic relationship of geological units to one another (Sefton-Nash et al., 2020). Specifically the DEM was used to create topographic profiles between the two areas of interest, using the associated tool in the web-GIS application called the Multi-Mission Geographic Information System (MMGIS), part of the larger suite of tools forming NASA's Advanced Multi-Mission Operations System which was used to access the DEM used (Calef et al., 2017, 2020). While not an integral part of the mapping effort, this was used where there is a question over whether the local stratigraphy matched up with what had been identified in previous studies i.e. that the Blue Subunit overlies the Orange Subunit (Mandon et al., 2021).

2.1.1. Using CaSSIS band ratio composites (CBRCs) to assess ferric-ferrous components

In addition to using standard CaSSIS R-G-B colour combinations to differentiate the two subunits, CBRC products (Tornabene et al., 2018; Tornabene et al. on prep) are used here to augment the identification and differentiation of the two subunits. Band ratioing involves dividing one image band by another on a pixel by pixel basis, with this acting to enhance the spectral differences within an image. Band ratioing also acts to reduce some of the effects due to variable atmospheric and topographic related illumination changes between observations. This method has seen frequent use, with HiRISE-CRISM comparisons of Martian terrain (Chojnacki et al., 2011; Sacks et al., 2020), along with the Landsat and ASTER instruments on Earth (van der Meer et al., 2012) being examples of this.

Tornabene et al. (2018) showed that specific CaSSIS band ratios can be used to distinguish the relative proportions of ferric and ferrous minerals. These readily highlight the wider Clay-bearing Unit at Oxia Planum (Tornabene et al., 2018). These CBRCs show distinctive yellow and orange colours for areas that are ferric-bearing, which is strongly correlated with areas that are clay-bearing based on CRISM hyperspectral targeted observations (Mandon et al., 2021; Tornabene et al. in prep). Exposures of the Blue Subunit also appear less ferric and are often bluer or cyan in the CaSSIS CBRC images, which would be expected if fayalitic olivine were mixed in with the clay.

In this study we utilised the CBRC NPBb product (Tornabene et al. in prep), consisting of the NIR/BLU (N/B), PAN/BLU (P/B) and PAN/NIR (P/N) band ratios in the R-G-B channels. The N/B and P/B ratios highlight minerals with a strong ferric absorption short of 550 nm by producing higher ratio values for minerals that are dominated by ferric iron over ferrous iron, while P/N highlights minerals with a strong ferrous absorption near 1000 nm. An example of the CBRC NPBb product is demonstrated in Fig. 5, along with a CRISM targeted D2300 spectral parameter (Viviano-Beck et al., 2014) map which highlights the presence of Fe/Mg-rich phyllosilicates. Within this comparison it is seen that those areas which registered as ferric within the CBRC NPBb product, i.e. those which have relatively higher values in the N/B and P/B ratios in comparison to the P/N ratio and therefore appears yellow, match very well with those areas that showed Fe/Mg-rich clay mineral detections within the CRISM products.

2.2. Differentiating and mapping the clay-bearing subunits

Mapping was carried out at a 1:6000 scale for the CaSSIS data and at 1:2000 for HiRISE, though lower scales of up to 1:1000 for HiRISE were used when there was difficulty determining the extent of fracturing present. An area would be observed using both data sets concurrently, with exposures of the Clay-bearing Unit being manually identified and classified as either of the subunits based on the colour and ferric-ferrous content of the exposure in the CaSSIS base and CBRC products, with HiRISE imagery used to determine the exact extent of the exposure. In the base and CBRC products, Orange Subunit exposures needed to appear orange-yellow in base CaSSIS imagery and yellow in the CBRC NPBb product, i.e. having a high value in the N/B and P/B ratios in comparison to the P/N, denoting a strong ferric signature. In contrast, the Blue Subunit needed to appear blue in base CaSSIS imagery and a very faint yellow-cyan in the CBRC product, i.e. having a lower value in the N/B and P/B ratios in comparison to the P/N ratio, denoting a more ferrous mineralogy.

In those cases where the colour of the exposure in the base CaSSIS image did not match what would be expected given its appearance in the associated band ratioed product (Fig. 6), or where exposures of the two subunits were present and too intermixed to reliably differentiate at the scale mapping was carried out, an additional category named "Indeterminate" was used. See Fig. 7 for an example of the mapping with exposures of the two subunits present, along with where the Indeterminate
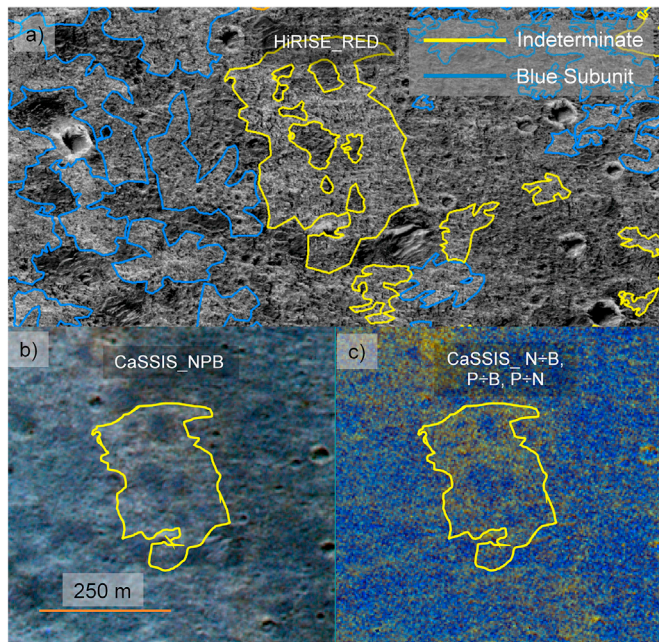
Fig. 6. Example "Indeterminate" exposure (centre of (a)), with the Indeterminate category being used in this case due to the exposure being distinctly blue in base CaSSIS imagery (b), indicative of the Blue Subunit, but having a reasonably strong ferric signature in the CBRC product (c), which matches what would be expected for the Orange Subunit. (a) HiRISE image [ESP_037558_1985], with mapping of the subunit exposures in the area being overlaid (b) Base CaSSIS image [MY35_008275_165_0]. (c) CBRC NPBb product based on CaSSIS image [MY35_008275_165_0]. See Fig. 3 for the location of this area within Oxia Planum.

category was used due to the close spacing of the units. The stretch used for both the base and band ratioed CaSSIS imagery was optimised linear stretch, a linear stretch calculated by ENVI as outlined in (Geospatial, 2021). This is what is used within the CaSSIS images shown unless stated otherwise. Both the calculation of the band ratios and the Dark Subtraction (DS) correction operation (see section 2.4) were carried out in ENVI 5.3.

2.3. Fracture measurements within the clay-bearing subunits

Several exposures of the Clay-bearing Unit across the 3σ landing envelope of the Rosalind Franklin rover had the fracture networks present manually mapped out (see Fig. 8 for an example of this), with the fracture length distributions for these sites, along with the polygon areas formed by the intersecting fractures, being reported. This fracture mapping was undertaken using HiRISE imagery at a 1:200 map scale, with the fractures mapped manually via the window-sampling method. All fractures at least partially within a window of 50×50 m are mapped (Zeeb et al., 2013).

Eight sites' fracture properties were measured, four covering exposures of the Orange Subunit, and four covering exposures of the Blue Subunit. In order to compare between the fracture and polygon area distributions of the mapped sites, Kernel Density Estimation (KDE) graphs were utilised (Rosenblatt, 1956; Parzen, 1962). KDE is a graph type similar to a histogram in purpose although, rather than counting the number of data points within a given bin, each data point is treated as a separate function centred at the data point, known as a kernel function. These individual functions are then summed together to give the final distribution which is shown in the KDE graph (Zielinski et al., 2018), with this being done using the "Kernel Density Estimation" function within the R programming language (Maechler and Team, 2021a,b). For the KDE graphs used here the individual kernels followed the
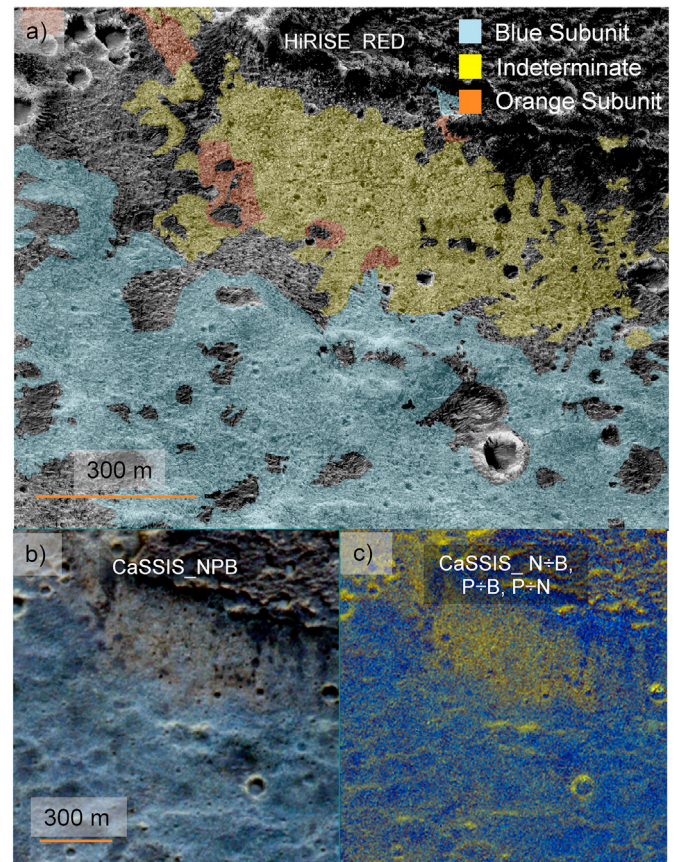

Fig. 7. Example of the clay subunit map, with deposits of the two subunits present. (a) HiRISE image [ESP_037558_1985], with mapping of the subunit exposures in the area being overlain. (b) Base CaSSIS image [MY35_008275_165_0]. (c) CBRC NPBb product based on CaSSIS image [MY35_008275_165_0]. Note the large Indeterminate unit exposure shown in (a), an example of where exposures of the Orange and Blue Subunits were too closely spaced to be differentiated reliably at the scale mapping was carried out. See Fig. 3 for the location of this area within Oxia Planum.

Epanechnikov function, while the bandwidth for each fracture site was determined using the bw.SJ bandwidth selector (Maechler and Team, 2021a,b), which uses pilot estimation of derivatives as outlined in (Sheather and Jones, 1991).

2.4. Errors and uncertainties in the data sets

From the calibration campaigns carried out both prior to its launch and after science operations began, the performance of CaSSIS has been well characterised. From the pre-launch calibration campaign (Roloff et al., 2017) various measurements were carried out to test and constrain the instrument's pre-flight performance. This included the creation of a flat-field map, identifying defective pixels and determining the detectors linear response, spectral response, and the bias levels and dark current of the detector. Calibration efforts carried out since the start of CaSSIS science operations (Pommerol et al. this issue, Thomas et al. this issue) also identified several artifacts which affect CaSSIS imagery, with these being issues related to stray light on the detector and variations in the bias of the detector.

Following these extensive calibration efforts the behaviour of the CaSSIS instrument has been well constrained, with both the absolute calibration of CaSSIS with relation to the Martian surface and relative calibration between CaSSIS products being shown to be very good. The well calibrated nature of the CaSSIS products used, along with the instruments high signal to noise ratios (SNR) across the four CaSSIS bands
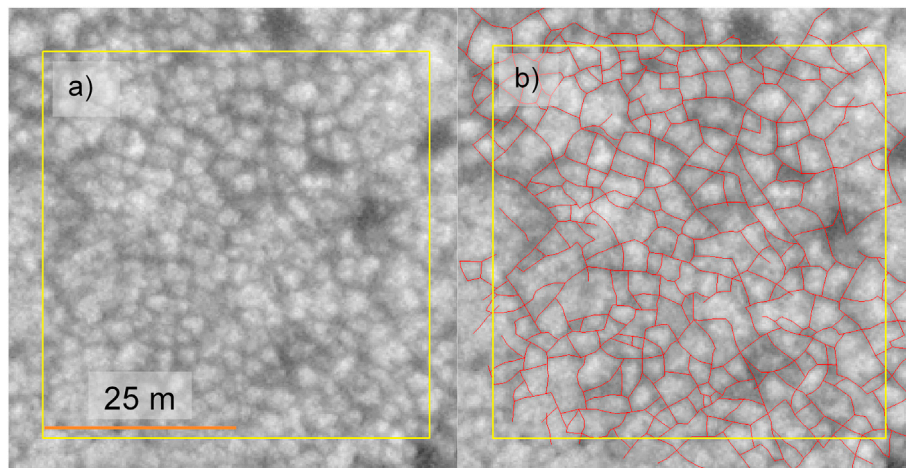
Fig. 8. Example of one of the fracture network maps created as part of this fracture mapping effort, with the Orange Subunit exposure both before and after mapping (a and b respectively) being shown. HiRISE image ID is [ESP_042846_1985]. See Fig. 3 for the location of this area within Oxia Planum.

of ~230 for PAN, ~160 for RED and NIR and ~110 for BLU at the top of atmosphere when the incidence angle is between 0 and 60° (Pommerol et al. this issue), means that CaSSIS is a reliable source of accurate multispectral data over Oxia Planum. However, this high colour sensitivity within CaSSIS images is reliant on several conditions which are not always fulfilled.

One of the foremost calibration issues with all Martian VNIR data sets over the range of 400–1100 nm is the lack of a standard atmospheric correction. This includes CaSSIS, which measures the I/F (incidence over flux) (Tornabene et al., 2018; Tornabene et al. in prep). I/F is heavily influenced by the photometric effects of time-variable aerosols scattering light in the atmosphere, with these aerosols affecting shorter wavelengths (those covered by the BLU and PAN filters) much more strongly than longer wavelengths (those covered by the RED and NIR filters) (Wolff et al., 2009). Therefore the scattering of atmospheric aerosols, in addition to reflections off the surface, contribute to the radiance detected at the sensor and thereby the overall shape of I/F spectra. This has been shown to influence the calculation of surface spectral properties, including band ratios (see Fig. 1 in (Fernando et al., 2016)). The magnitude of this impact on surface spectra by dust scattering is characterized by the optical depth of dust at the time of the image acquisition (τ_{dust}). This is especially an issue in the use of CBRCs; due to the aforementioned issues over the wavelengths covered by CaSSIS, high dust opacities act to increase the apparent ferric content of those areas so affected. It should also be noted that terrain which is in shadow also appears strongly ferric regardless of the composition of the shadowed terrain, another factor which needed corrections in this data set.

An empirical DS correction, commonly used in remote sensing applications (Chavez, 1988; Daubar et al., 2016; Munaretto et al., 2020), is recommended for CaSSIS prior to band ratioing and spectral analysis (Tornabene et al., 2018). The DS correction simply determines the minimum value of each band and subtracts that value from said band. In order for this correction to be properly applied and effective, the subtracted minimum values must originate from a shadowed pixel where the signal is dominated by scattering with minimal contribution from the surface. Consequently DS is a scene-dependant correction (i.e., the presence of shadows is dependent on illumination and topographic conditions) that does not always work properly, so caution is advised when using this technique and interpreting the resulting DS-corrected I/F spectra. Furthermore the image must have sufficiently high SNR and estimated dust and water-ice opacity values should be < 1.0 and 0.2, respectively (Tornabene et al., 2018; Tornabene et al. in prep). Indeed the DS correction is only partially effective at isolating the surface signal for images taken when dust opacity was higher than one. This is the case for one of the four images used in this study, with this image being used

to map ~23.3 km^2 i.e. 14% of the area mapped in this study. See Fig. 9 for a comparison of this high dust opacity image with an overlapping low dust opacity one.

Current observations of the Martian atmosphere indicate that there is a distinct, generally repeatable pattern for levels of water-ice aerosols over the Martian seasons (Smith, 2008; Wolff et al., 2009). During Mars aphelion water-ice opacity can vary between 0.05 and 0.5 over a latitude range of ~ -10 to +30° (Smith, 2008). From observations made of the variation in the water-ice opacity over Mars from (Smith, 2008; Wolff et al., 2019), it can be seen that the water-ice opacity over Oxia Planum is generally negligible, and consequently is not considered an issue within this study.

Dust opacity for each CaSSIS image is considered by using an extension of the assimilation of the Open access to Mars Assimilated Remote Soundings (OpenMARS) dataset (Holmes et al., 2020). The sensitivity of CaSSIS to dust also extends to dust on the surface. The CaSSIS P/B ratio is designed to highlight pixels with an absorption over the blue-green wavelengths associated with ferric iron, but does not necessarily differentiate well between ferric-bearing clays and ferric-bearing dust. From previous characterisation of the landing site it was shown that Oxia Planum was sufficiently dust-free to be an acceptable site for the ExoMars mission (Westall et al., 2014; Quantin-Nataf et al., 2017), while the extensive clay deposits detected from scanning CRISM and OMEGA data (Carter et al., 2016) would not have been detectable if there were significant dust coverage at this scale of mapping i.e. at the 100 m scale. While this indicates that Oxia Planum has relatively low dust coverage at the regional scale (Ruff and Christensen, 2002), the high resolution at which the mapping in this paper was undertaken means that there is still the possibility for significant surface dust-derived obfuscation.

Where there is overlapping coverage between the high resolution CRISM targeted data and CaSSIS imagery, it can be seen that there is a clear correlation between those areas which have strong Fe/Mg phyllosilicate detections within the CRISM data and those which are ferric in CBRC products, with no examples of false positives which could not be attributed to slope-effects. This is an encouraging indicator for the presence or lack thereof for significant dust at the scale the mapping in this paper was undertaken, given that those CRISM spectral signatures of Fe/Mg phyllosilicates would have been masked by the presence of even a very thin coating of dust.

Another consideration with CaSSIS is that, as its orbit is not sun-synchronous, the varying lighting conditions from image to image could significantly affect the SNR of the imaged area. From the latest CaSSIS calibration efforts (Pommerol et al. this issue) it was shown that beyond a solar incidence angle of ~60°, lowering solar flux leads to drops in the SNR across all four image filters as the contribution of atmospheric
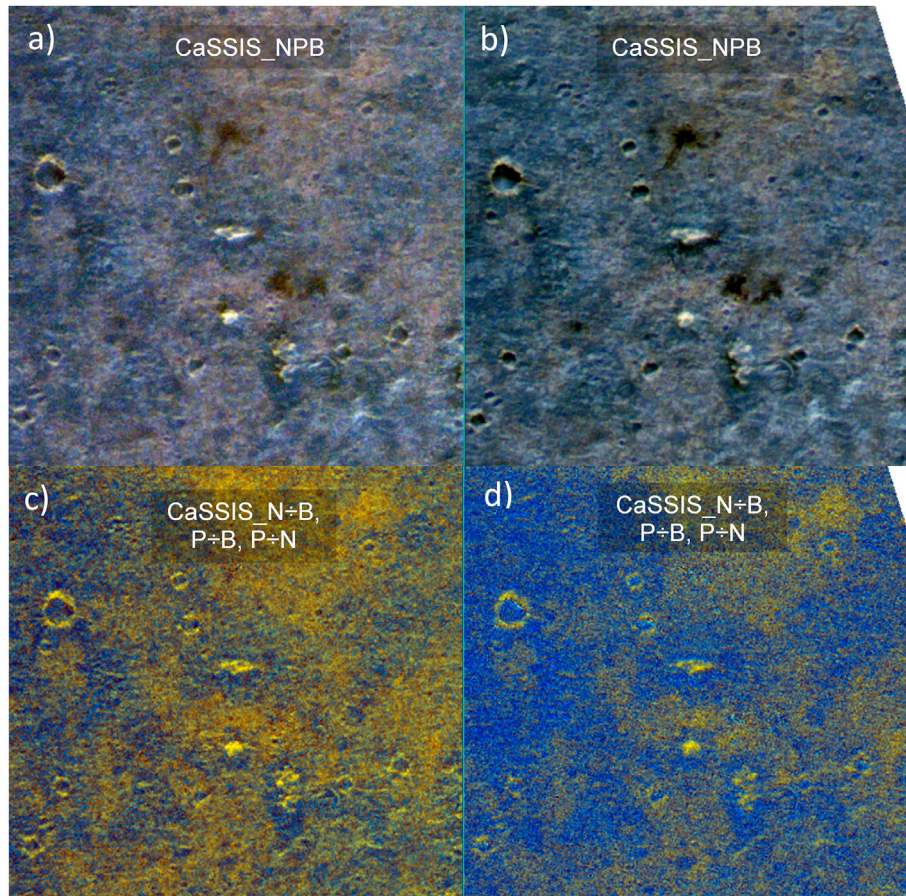
Fig. 9. Comparison between the base (a) and CBRC (c) CaSSIS image [MY34_003806_019_2], which has a high dust opacity of 1.21, and the corresponding base (b) and CBRC (d) CaSSIS images of [MY35_008275_165_0], which has the low dust opacity of 0.4. Location pictured is at 24.38 W 18.21 N. See Fig. 3 for the location of this area within Oxia Planum.

scattering to the signal increases significantly. Of the images used in this study only one, MY35_006504_018_0, has a solar incidence angle greater than 60° (74.9°, see Table 1), with the area mapped using this image being ~10.3 km^2 (6.3% of the total). Consequently any issues related to varying lighting conditions is not viewed as a significant issue in this study.

With respect to the HiRISE instrument, while it possesses a relatively poor absolute calibration with an accuracy of ~20%, its relative pixel-pixel calibration is very good (at ~1–2% pixel accuracy) (Milazzo et al., 2015). This was deemed to be sufficient for our study. Additionally, as the orbit of HiRISE is sun-synchronous, lighting conditions do not vary significantly as is the case with CaSSIS, meaning it is a negligible issue for HiRISE.

3. Results

3.1. Map of the clay-bearing subunits

The results of our mapping within the 1σ+ landing envelope are shown in Fig. 10. From those areas mapped i.e. the ~91% of the 1σ+ envelope which had CaSSIS coverage, it can be seen that in total ~18% of the 1σ+ envelope is covered by exposures of the Orange Subunit, ~9% by exposures of the Blue Subunit, and ~12% by clay exposures which could not be conclusively classified as either (Indeterminate). It can be seen that there are differences across the landing site with respect to the exposure and distribution of the two clay-bearing subunits. The south-east half of the 1σ+ landing envelope (see (a) in Fig. 10 and an example of the area in Fig. 12a, c and e) is dominated by exposures of the Orange Subunit with ~70% of the clay exposures belonging to this

subunit. Exposures of the Blue Subunit are also present at ~10% of overall clay exposure, with this being concentrated in the southern tip of the landing envelope. The north-west half of the landing envelope (see areas (b), (c) in Fig. 10 and an example of the area in Fig. 12b, d and f) in contrast has a more equal distribution of the two clay-bearing subunits, with there being significant exposures of both present at 22% for the Orange Subunit and 37% for the Blue Subunit.

While the clay-bearing subunits are widespread across the majority of the 1σ+ envelope, how well exposed these subunits are varies across the landing site. In the south-western half of the landing envelope ((a) in Fig. 10) the Clay-bearing Unit appears well exposed with extensive fracture networks being visible, distinct colouration when compared to the surrounding units and possessing relatively few occurrences of the DMU to obscure the underlying Clay-bearing Unit (see Fig. 12a–c). This area is also relatively free from features such as Transverse Aeolian Ridges (TARs) (Silvestro et al., 2021), which also act to conceal the Clay-bearing Unit. The central portion of the landing envelope meanwhile ((b) in Fig. 10) has fracturing that, while still extensive, forms fewer large contiguous fracture networks in comparison to the south-western portion. Here we can also observe increased obfuscation of the Clay-bearing Unit by the DMU and TARs (see Fig. 12b, d and f) for a representative example. The northern portion ((c) in Fig. 10) is primarily split between several large exposures, though the presence of extensive TARs towards the northern tip of the envelope and the DMU mean that it is not as well exposed as the south-western portion of the landing envelope.

Comparing between the point mapping carried out by Mandon et al. (2021) (see Fig. 11) and the results presented here, there are some disagreements over which subunits are present within a given 1 × 1 km^2
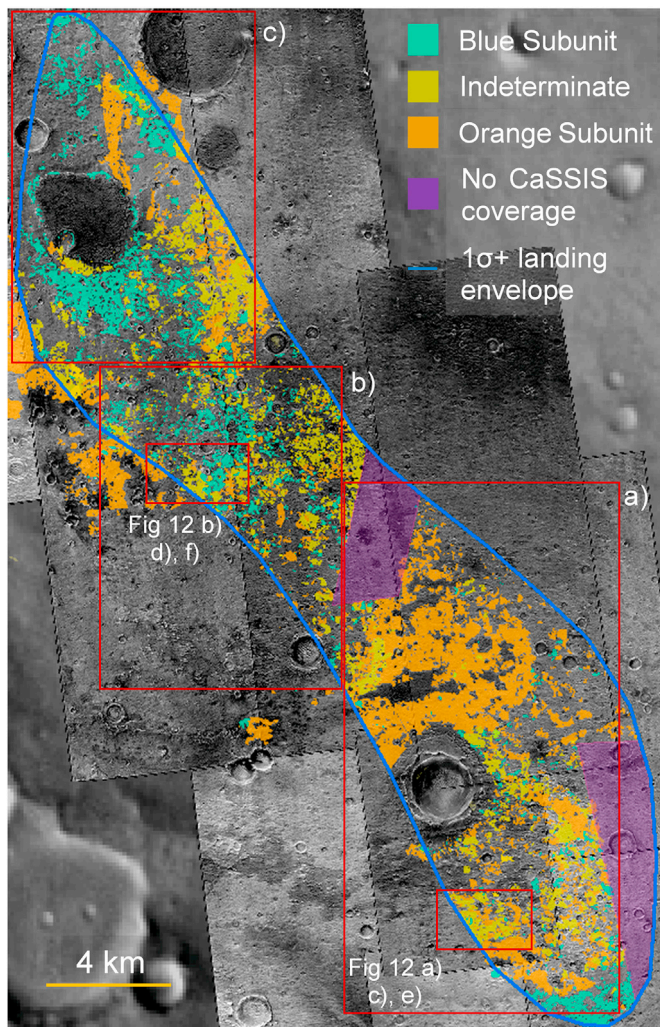
Fig. 10. Map of Orange, Blue and Indeterminate clay subunit exposures across the 1σ+ landing envelope. Those areas that do not clearly belong to the Clay-bearing Unit have been left unmarked. This includes areas which belong to another unit, such as the DRU and DMU, areas with dust or TAR coverage heavy enough to obscure the underlying terrain, and those areas which do not have the fracturing or colouration indicative of the clay-bearing subunits. Of the 163 km² area mapped out, 28.5 km² was covered by Orange Subunit exposures, 14.8 km² by Blue Subunit exposures and 17.8 km² by exposures classed as Indeterminate.

Fig. 11. Map of the Orange and Blue Subunit exposure detections, summarised at a 1 × 1 km scale, from Mandon et al. (2021). The data shown is limited to the 1σ+ envelope.

area. However this outcome is to be expected, given the different approaches to mapping between this earlier work and what is undertaken here. One possible source of disagreement is the use of an "Indeterminate" category in this study, opening up the possibility of an area which had been identified as belonging to one subunit previously being marked as this category here, and thus confusing any direct comparison between these studies. More broadly however, within Mandon et al. (2021) the aim of subunit mapping was to identify subunit exposures across the breadth of the landing site for analysis and to provide a first-order idea of how the distribution of the two subunits varied across the landing site. It was not aiming to create a comprehensive map of these subunit exposures. This contrasts with the efforts shown here, which aimed to provide a more detailed and comprehensive map of the two subunits across the 1σ+ landing envelope.

From the observations which were carried out on areas not previously observed in high resolution colour imagery, several new facts were noted. Two examples of "fluvial deposits" present within the 1σ+ envelope (Quantin-Nataf et al., 2021) were found to contain no exposures of the Blue Subunit. This would suggest that the differentiation of the Clay-bearing Unit occurred prior to the formation of the channels at the
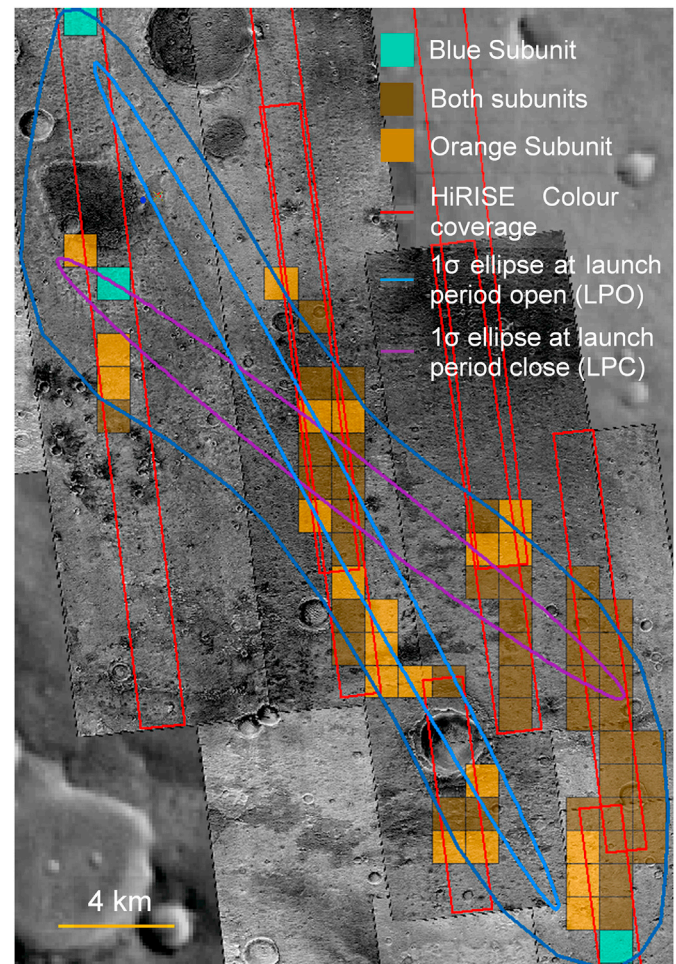
site, and that the channels subsequently eroded through the Blue Subunit to expose the underlying Orange Subunit. The greater coverage provided by this map has also highlighted a greater presence of clay-bearing material within the NW of the 1σ+ landing envelope than had been known previously. In comparison to earlier mapping by Carter et al. (2016) our work has helped to constrain those areas where the Clay-bearing Unit is easily accessible at the surface.

It should be noted that the only CaSSIS coverage over a large section of the central portion of the landing envelope was provided by CaSSIS image MY34_003806_019_2, which had a high estimated dust opacity (1.21). Given the issues mentioned in Section 2.4 with regards to DS correction being insufficiently effective for high dust opacity images, increased scattering from dust in the atmosphere would have given the terrain covered by this image a higher ferric content than is actually present (see Fig. 9 for a comparison between where this high dust opacity CaSSIS image overlaps another with a lower dust opacity). This likely explains in part the high percentage of the Clay-bearing Unit marked as Indeterminate in the area covered exclusively by this image (60%), compared to the Orange Subunit (~27%) and the Blue Subunit (~11%), as well as the corresponding percentage in the north-west half of the landing envelope (~41% marked as Indeterminate).

During the course of mapping out the Clay-bearing Unit, the relative elevations of the clay-bearing subunits to each other and to other units present at Oxia Planum were observed, with this being done using topographic profiles generated using the combined HiRISE-CTX DTM. With respect to each other it was seen that, where the two subunits were in contact, the Blue Subunit had a higher elevation than the Orange
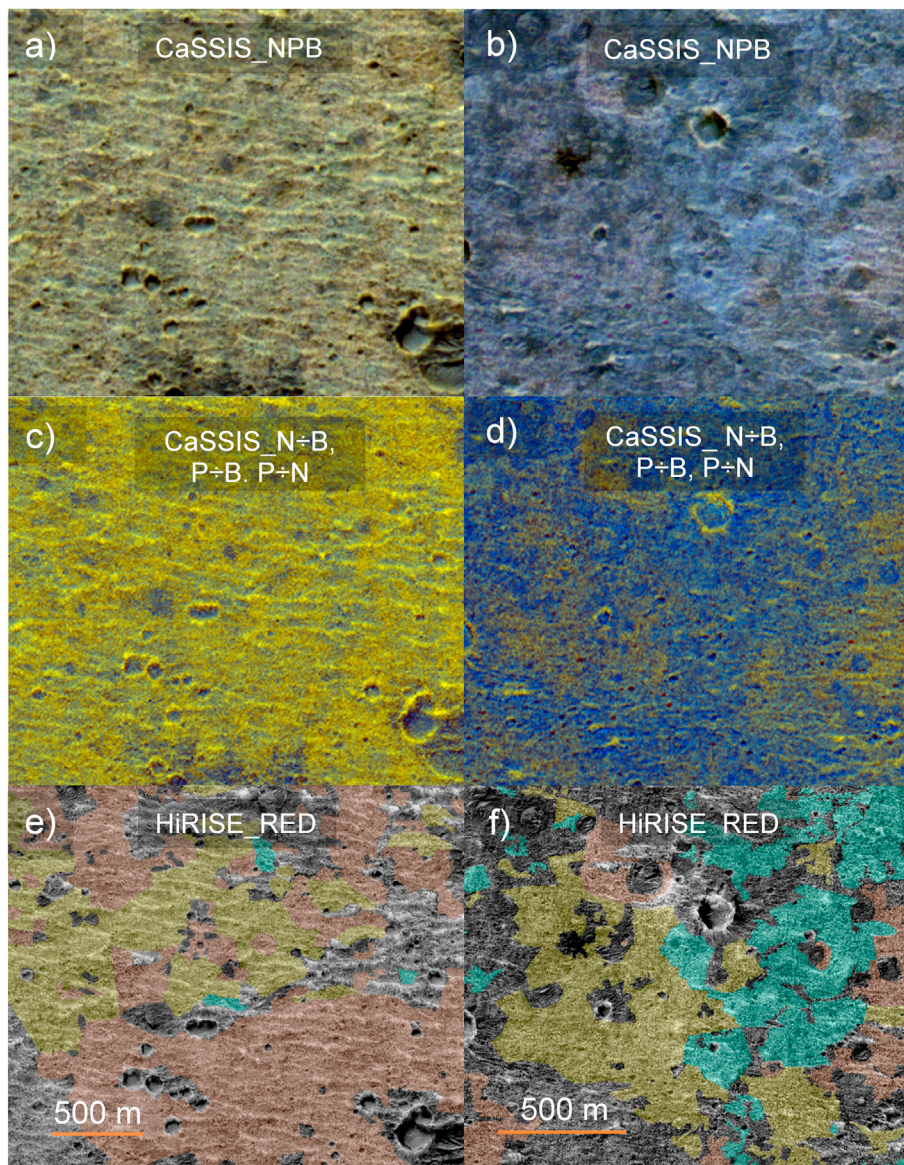
Fig. 12. Two examples of terrain typical of the SE (a, c, e) and NW (b, d, f) of the landing envelope, with a base CaSSIS image (a, b), CBRC (c, d) and HiRISE mosaic (e, f) being shown. The subunit map for each example area is overlain onto the respective HiRISE mosaics, with the colour scheme, and the corresponding units, being the same as used in Fig. 10. CaSSIS image IDs are: [MY35_009481_165_0] (a, c) and [MY35_008275_165_0] (b, d). HiRISE image IDs are: [ESP_042701_1980] and [ESP_045167_1980] (e), [ESP_037558_1985] and [ESP_047501_1985] (f). See Fig. 10 for the locations of these sites within Oxia Planum.
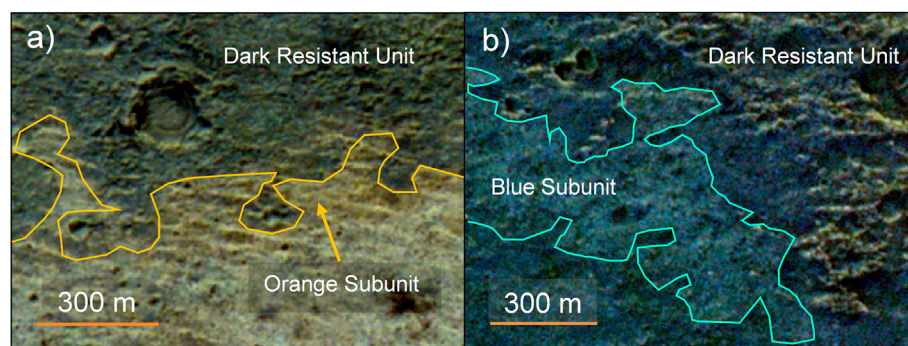

Fig. 13. Examples of where the Dark Resistant Unit (top of image in (a), right of image in (b)) appears to overlay exposures of the Orange Subunit (centre of image in (a)) and Blue Subunit (centre of image in (b)). CaSSIS image IDs are [MY35_009481_165_0] (a) and [MY34_005012_018_2] (b). These images are located at; 24.28 W 18.05 N (a), 24.049 W 17.96 N (b). See Fig. 3 for the locations of these sites within Oxia Planum.

Subunit and thus appeared to overlay the Orange Subunit in the stratigraphy. This matches with what has previously been identified in Mandon et al. (2021). Additionally exposures of the DRU were found to directly overlay outcrops of both the Orange and Blue Subunits (see Fig. 13). While this had previously been posited in Mandon et al., (2021), it had not been demonstrated.

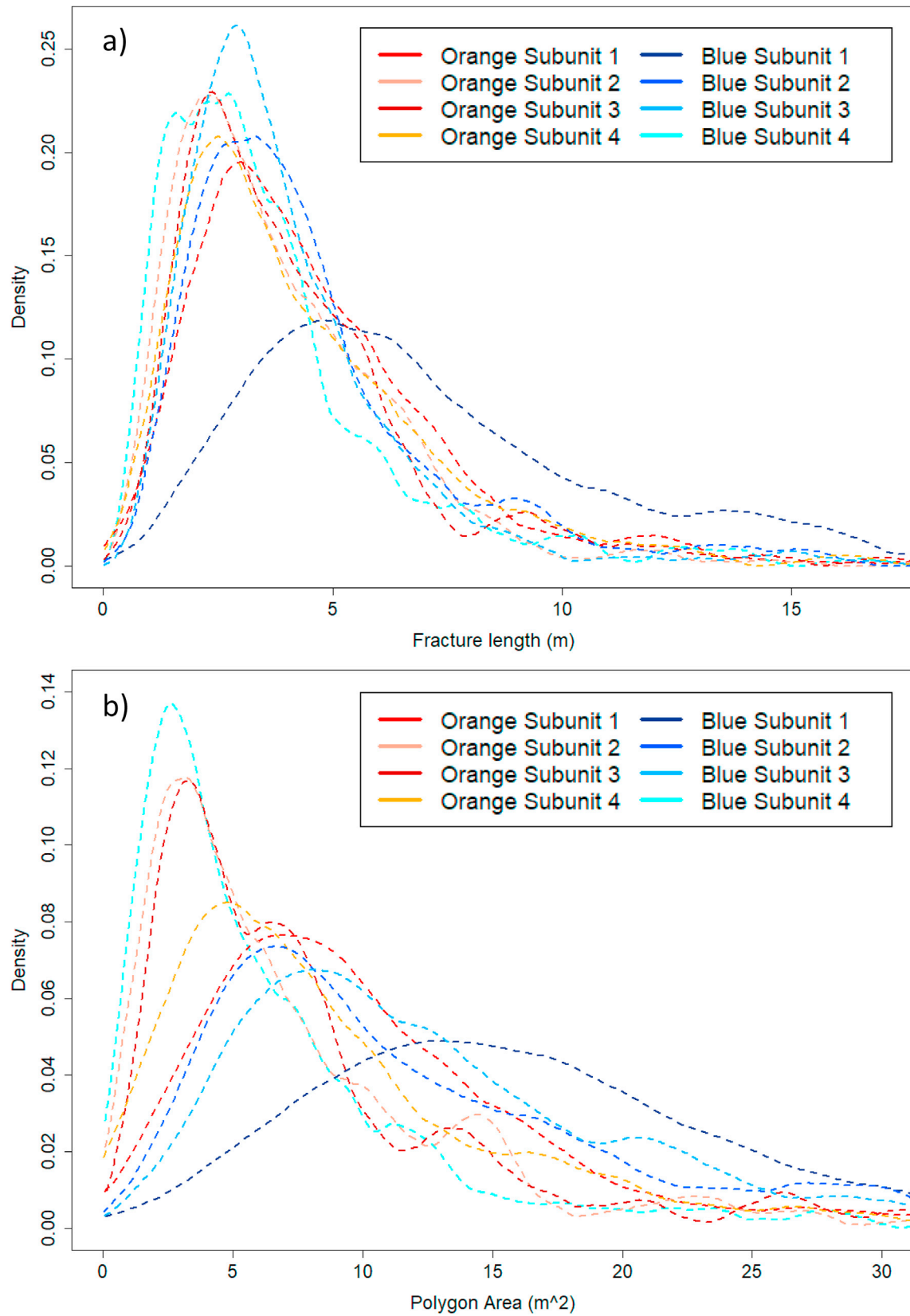**Fig. 14.** Kernel Density Estimation graphs showing the fracture length distributions and the polygon area distributions for several clay exposures in (a) and (b) respectively. These sites are located at; 23.65 W 17.93 N (OS1), 23.91 W 17.71 N (OS2), 24.53 W 18.28 N (OS3), 24.43 W 18.16 N (OS4), 23.91 W 17.88 N (BS1), 24.17 W 17.90 N (BS2), 24.21 W 17.90 N (BS3). See Fig. 3 for the locations of these sites.

3.2. Fracture measurements

The variation in both colouration, fracturing and texturing within the 1σ+ envelope for the most part matches or at least does not contradict what has been identified previously for the 3σ envelope (Mandon et al., 2021). There is one notable exception: previously it had been suggested that fracturing within the Blue Subunit was limited to decametre-scale fracturing, in contrast to the Orange Subunit which possessed metre to decametre-scale fracturing. However, during the course of constructing this map, it was found that metre to decametre scale fracturing could be found across both subunits with examples of metre-scale fracturing in the Blue Subunit being shown in Fig. 15.

This finding was also borne out by the fracture length and polygon size measurements made during the fracture mapping of the Orange and Blue clay-bearing subunits (see Fig. 14 and Table 2). Here it can be seen that fracturing was primarily at the metre scale within the Blue Subunit, though the "Blue Subunit 1" site possesses broader distributions that peak at higher values for both metrics compared to the other sites. The polygon area for this example of the Blue Subunit was primarily >10 m^2, though examples of polygons with areas less than 10 m^2 were present. In contrast the other Blue Subunit sites looked at had very similar fracture length and polygon area distributions to those seen within the Orange Subunit. From the observations of the Blue Subunit during mapping it is therefore concluded that the presence of exclusively, or at least primarily, decametre-scale fracturing should not be seen as a feature of the Blue Subunit. Instead the fracturing present within the Blue Subunit is primarily metre-scale.

4. Discussion

4.1. Differences between the clay-bearing subunits: mineralogical or differences in exposure

The processes which caused the apparent differentiation within the Clay-bearing Unit to form its subunits is currently uncertain, with two broad hypotheses being put forward to answer this (Mandon et al., 2021). The first, and the one favoured by the authors of that study, is that compositional and mineralogical differences between the subunits, whether resulting from processes in the Clay-bearing Unit which altered the material post-deposition or differing detrital source material, explain the difference in colouration and spectra that these two subunits exhibit. The second is that there are no compositional differences between the two subunits, with the suggested cause of the differing colour and spectra being differences in dust coverage.
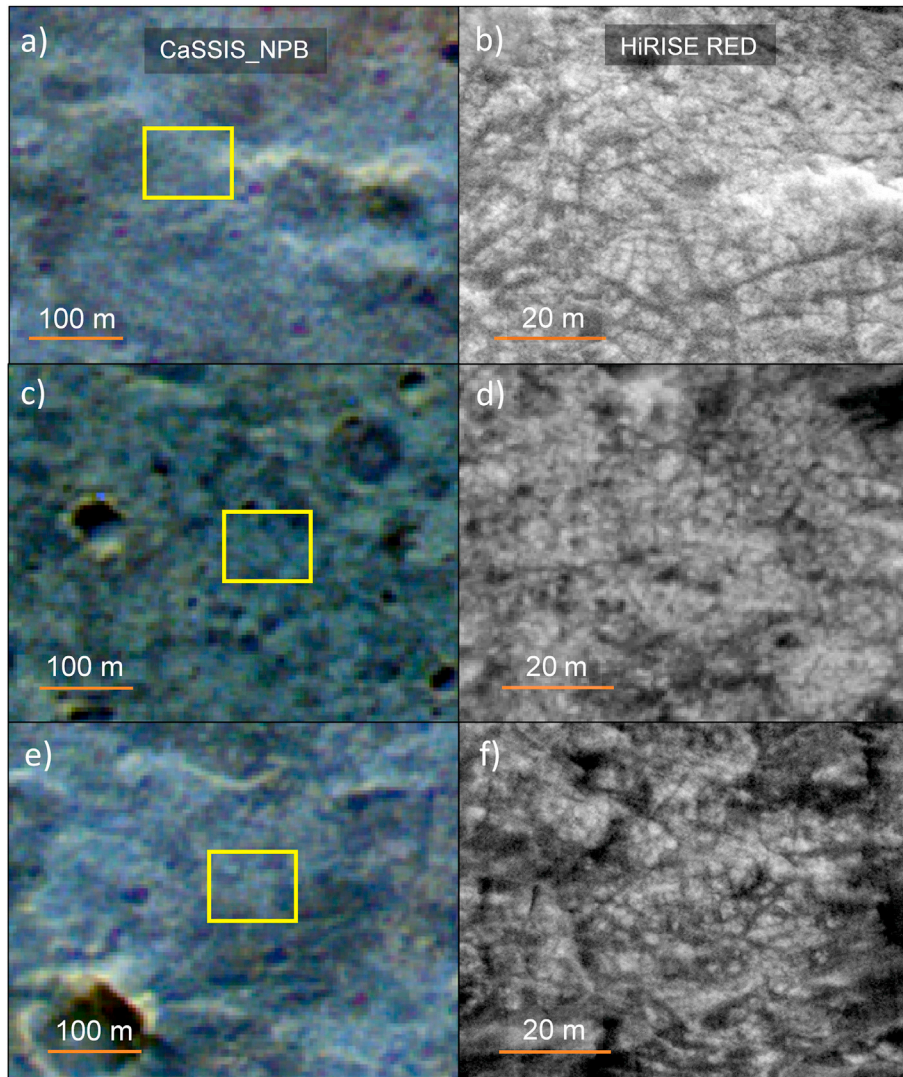
Fig. 15. Examples of the Blue Subunit in both CaSSIS (left) and HiRISE (right) imagery, showing distinct metre-scale fracturing. The yellow boxes indicate locations of the respective right-hand panels. These are located at; 24.45 W 18.25 N (a, b), 24.19 W 17.90 N (c, d) and 24.38 W 18.16 N (e, f). The image IDs are [MY35_008275_165_0] (a, e), [MY35_009481_165_0] (c), [ESP_037558_1985] (b, f) and [ESP_045167_1980] (d). See Fig. 3 for the locations of these areas within Oxia Planum.

Table 1

List of the images used in this study along with relevant characteristics.

Image ID	Instrument	Latitude (°)	Longitude (°)	Local time	Incidence angle (°)	Phase angle (°)	Emission angle (°)	Optical Depth (τ)
MY34_003806_019_2	CaSSIS	17.95	335.58	09:51	53.1	60.6	11.1	1.21
MY35_006504_018_0	CaSSIS	17.87	335.74	06:51	74.9	72.9	13.2	0.51
MY35_008275_165_0	CaSSIS	18.5	335.49	10:56	16	24.4	11.7	0.4
MY35_009481_165_0	CaSSIS	18.21	335.71	13:42	24.4	31.7	11.3	0.44
ESP_037558_1985	HiRISE	18.21	335.58	15:46	57	41.8	15.4	N/A
ESP_040433_1985	HiRISE	18.14	335.76	14:12	50	64.8	18.3	N/A
ESP_042701_1980	HiRISE	17.98	335.74	14:44	39	39.5	0.2	N/A
ESP_045167_1980	HiRISE	17.86	335.83	15:07	44	42.7	1.5	N/A
ESP_047435_1985	HiRISE	18.06	335.82	15:16	59	58.7	0.5	N/A
ESP_047501_1985	HiRISE	18.29	335.67	15:22	61	42.3	21.3	N/A
ESP_050560_1980	HiRISE	17.8	335.76	14:11	36	30.1	6.8	N/A

Table 2

Metrics of the different fracture sites mapped over 50 × 50 m areas in HiRISE images. See Fig. 3 for the locations of these sites within Oxia Planum.

Clay exposure	Mean fracture length (Standard Deviation) [m]	Mean polygon area (Standard Deviation) [m^2]	Number of fractures (number below 10 m)	Number of polygons (number below 10 m^2)	ID of HiRISE image used for mapping
Blue Subunit 1	8.5 (7.6)	18.3 (11.6)	200 (146)	163 (32)	ESP_019084_1985
Blue Subunit 2	4.7 (3.2)	12.9 (10.0)	391 (368)	205 (105)	ESP_045167_1980
Blue Subunit 3	4.0 (2.6)	12.9 (7.6)	350 (338)	178 (77)	ESP_045167_1980
Blue Subunit 4	3.8 (2.8)	8.6 (13.1)	400 (381)	197 (155)	ESP_039721_1980
Orange Subunit 1	4.7 (2.9)	10.8 (7.7)	356 (334)	212 (112)	ESP_042846_1985
Orange Subunit 2	3.9 (2.4)	8.1 (8.1)	410 (401)	236 (170)	ESP_051417_1980
Orange Subunit 3	4.8 (4.8)	9.5 (10.3)	379 (322)	218 (154)	ESP_057681_1985
Orange Subunit 4	4.5 (3.3)	10.5 (10.6)	336 (313)	183 (117)	ESP_057681_1985

Our results from this mapping effort also favour the first of these two hypotheses. This is partly due to the observation of the consistent stratigraphic relationship of the Orange Subunit to the Blue Subunit observed across the landing site, with the Orange Subunit being found to be lower in the stratigraphy than the Blue Subunit wherever exposures of the two are found adjacent to each other. This matches what was described by Mandon et al. (2021). If an olivine-bearing superficial material was responsible for the apparent differences in colour/spectra, the stratigraphy of the two subunits could be expected to be reversed, given that the Orange Subunit is frequently found in topographic lows where superficial material could be expected to collect. Conversely, if it were a clay-bearing superficial material causing this apparent difference, it would be expected that dust traps such as the crater floors would possess a strong ferric signature, which is not observed.

In addition to this, both of the clay-bearing subunits have been found to be in direct contact with overlying deposits of the DRU where this unit has eroded back, as evidenced in Fig. 13. It has also been observed that two previously identified fluvial channels which lie within the $1\sigma+$ envelope (see Fig. 1 for the location of both, and Fig. 16 for an example), appear to have clear exposures of the Orange Subunit at the base of them with no visible Blue Subunit exposures. This would imply that these channels were formed after the differentiation of the two subunits, having eroded through the overlying Blue Subunit and in the process exposing the underlying Orange Subunit. While the latter two points in isolation could be explainable by specific variations of dust coverage, when taken together these three points argue against the idea that differences in the colours and spectra between the two subunits are due to varying levels of exposure and-or levels of dust coverage.

4.2. Implications of mineralogical variation

Given that the differences between the two subunits are thought to be mineralogical in nature, the question of what process led to the subunits differentiation arises. This is heavily dependent on several factors, including the length of time water was present at the site, along with what mechanism initially caused the formation of the Clay-bearing Unit.

From the clay candidates identified in Carter et al. (2016) and Mandon et al. (2021), some possibilities about the nature of the hydrological environment at the time of clay formation arise. On Earth vermiculite often forms in the unsaturated zone above a site's water table (Bush et al., 2001) via chemical weathering or hydrothermal alteration (Weaver and Weaver, 1973; RRUFF-Project, 2001a,b; Velde and Meunier, 2008); while saponite forms either in alkaline evaporitic lakes, via weathering of mafic-ultramafic rocks, or via hydrothermal action within veins and vesicles of volcanic rock (RRUFF-Project, 2001a,b; Huang et al., 2013).

Conclusively identifying which mineral species the clays at Oxia Planum belong to will help constrain the past environment of Oxia Planum, as well as their geological setting when investigated by the Rosalind Franklin rover. If the clay proves to be a vermiculite, this would suggest that Oxia Planum was above the groundwater level at the time of clay formation but had significant circulation of water ongoing (Bush et al., 2001). If the clay was determined to be a saponite it might suggest a setting within a more transient, alkaline standing body of water (Velde and Meunier, 2008; Huang et al., 2013).

However, both vermiculite and saponite can form via the weathering of olivine (Delvigne et al., 1979, Bush et al., 2001), though olivine has only been detected within the Blue Subunit (Bristow et al., 2021). Of the materials identified to make up these subunits, the instability and varying weathering rate of olivine makes its presence of particular interest. In terms of the environment lower temperatures (Stopar et al., 2006), water of near-neutral pH (Wogelius and Walther, 1992), or water of neutral-basic pH under medium to high partial pressure of CO_2 (Wogelius and Walther, 1991), all act to retard olivine alteration. The properties of a specific olivine exposure itself also affects this, with larger grain size and more forsteritic olivine acting to reduce the weathering rate (Stopar et al., 2006). Depending on the combination of these factors, olivine can be expected to last at the surface when exposed to water for anywhere from decades to millions of years, with lifetimes of potentially 100's of millions of years under ideal conditions e.g. large-grained forsteritic olivine exposed to low temperature ($-50\ °C$) brines (Stopar et al., 2006; Olsen and Rimstidt, 2007). Achieving a greater understanding of how olivine varies across the two subunits, as well as further constraining the
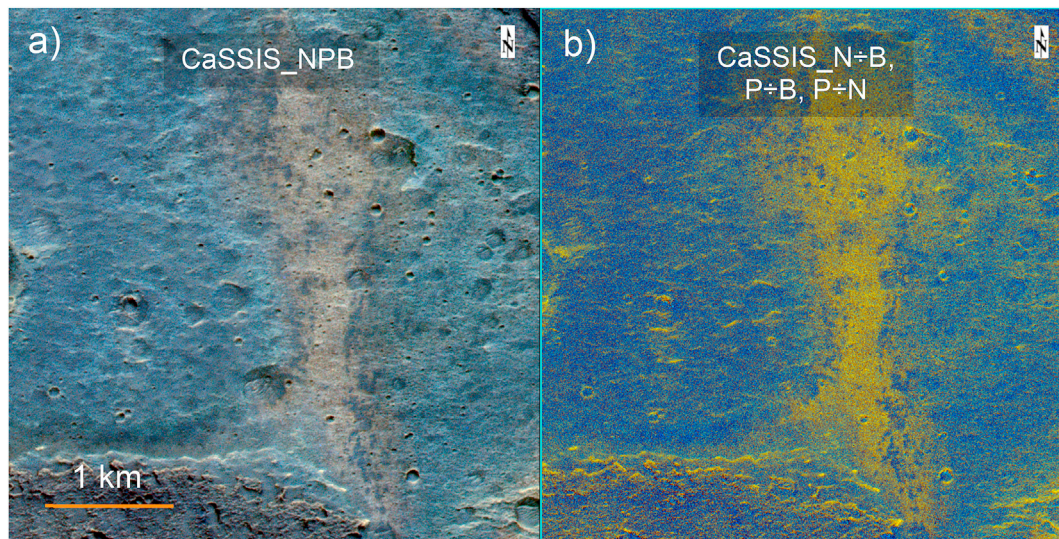
Fig. 16. Example of one of the channels, with this instance located in the north-west of the 1σ+ landing envelope. Flanked by Blue Subunit exposures, the channel itself can be distinctly seen to consist of an Orange Subunit deposit in both the base CaSSIS image (a) and CBRC (b). The image ID is [MY35_008275_165_0].

mineralogy of the Clay-bearing Unit, will help narrow down the potential histories of the site, and ultimately be key to understanding the extent and nature of water-rock reactions at the site.

If it was discovered that olivine content within the Clay-bearing Unit decreases with depth, as proposed by Mandon et al. (2021), potentially including detecting trace amounts of olivine within the Orange Subunit, this would indicate either that olivine had been altered after emplacement via diagenesis or pedogenesis, or that the olivine percentage of any incoming sediment varied. By tracking any such variation in olivine content, it could be possible to determine how the environment changed at the site, or changing sediment sources into Oxia Planum. A corresponding increase in the percentage of clays with depth would also be an indication that the olivine within the unit was the unaltered originator of the clay mineral present. Such a process could be similar to what has been suggested for the Clay Unit at Gale Crater where thermochemical modelling, based on mineralogical and compositional data determined by the Curiosity instruments, have indicated that low temperature (<50 °C) diagenetic alteration of an amorphous and olivine-rich detrital material is responsible for the saponite clay present in the Sheepbed Member of the Bradbury Formation (Léveillé et al., 2014; Vaniman et al., 2014; Bridges et al., 2015). If this is the case it could be expected that the features related to these diagenetic episodes at Gale Crater, such as the presence of mm-sized solid and hollow nodules along with raised ridges formed by multiple layers of a cemented material for the early-stage diagenesis, or the sulphate-filled fractures from the later-stage diagenesis (Grotzinger et al., 2014; Léveillé et al., 2014; Rampe et al., 2020), could also be present at Oxia Planum.

If in contrast there was a sharp boundary between the two subunits, with no olivine present in the Orange Subunit and there being no significant variation in olivine content across the Blue Subunit, this would suggest that the olivine present was detrital and not directly related to the presence of clay within the unit. If the origin of the material making up the Clay-bearing Unit is detrital, this difference could be indicative of olivine being introduced into the Blue Subunit via changes in sediment from the extensive catchment area of the site. Nearby volcanic activity could also be responsible, with the olivine representing volcanic ash fall onto the site during deposition of the Clay-bearing Unit. Such a sharp transition could alternatively be indicative of a rapid change within the environment at the site, causing the weathering rate which had been high enough to remove any olivine present within the Orange Subunit to dramatically slow during the formation of the Blue Subunit.

Several potential scenarios for the formation of the Clay-bearing Unit have been put forward previously in Mandon et al. (2021) and

Quantin-Nataf et al. (2021). While the absence of ground level investigations of the site makes conclusively proving or disproving the different hypotheses impossible, there are further studies which could be carried out from orbit to narrow the likely formation mechanisms. If deposits which match the clay and olivine spectral signatures can be found within the catchment area of Oxia Planum, this would reinforce a potential detrital origin, with the reverse being true if this is not the case. Following the arrival of Rosalind Franklin however, constraining the presence of clay material and olivine within the Clay-bearing Unit will ultimately be key to identifying the circumstances of formation for this unit.

4.3. Origin of the fracturing within the Clay-bearing Unit

Given the significant variation in the environment of Oxia Planum over the history of the Clay-bearing Unit and its potentially deep burial (Quantin-Nataf et al., 2021), the origin of the fracturing within it is uncertain and difficult to ascertain. However, from what is known about the history of Oxia Planum, several possibilities present themselves. One of the formation mechanisms for the Clay-bearing Unit necessitates that it formed in a body of water whether in a palustrine, lacustrine or marine setting. Assuming this, and that the Clay-bearing Unit possesses a high enough percentage of clay minerals (Hashim et al., 2006), significant swelling could have occurred within the Clay-bearing Unit given the nature of vermiculite and saponite which swell when saturated with water (Olphen, 1965; Suquet et al., 1977; Yang et al., 2015). When the site dried out and by extension the Clay-bearing Unit, it would have shrunk and desiccation fractures could have formed. Another suggestion which has previously been put forward is that of hydraulic fracturing (Quantin-Nataf et al., 2021), with the potential burial of the Clay-bearing Unit to depths of up to ~1 km generating high enough pressures that hydraulic fracturing could occur (Caswell and Milliken, 2017), assuming water was present within the Clay-bearing Unit at this time.

Other potential mechanisms are possible but less likely based on the observable morphology of the fracture network or the history of Oxia Planum. One of these possibilities is syneresis, whereby changes in the salinity of water overlying or, in the case of ground water surrounding, a deposit causes the expulsion of water from the material followed by its shrinkage and fracturing (Scherer, 1989). However this is thought to be an unlikely mechanism in this case due to it only rarely forming fracture networks when observed on Earth (Plummer and Gostin, 1981). Another is thermal contraction cracking, a group of mechanisms whereby cycling of the temperature in a material cause stresses which fracture it (Levy

et al. 2008, 2009). However, as these tend to form very uniform fracture networks with fractures intersecting each other at 120°, unlike what has been observed at Oxia Planum during the course of this study, this again is thought to be unlikely.

From the examples of fracturing within the two subunits looked at it can be seen that, in general, there is a high degree of similarity between the fracture lengths and polygon areas between the two subunits. This would suggest that the two subunits are similar in specific ways in order to generate such similar fracturing, with which factors need to be similar depending on the formation mechanism of the fracturing. One factor that can have a significant effect on fracturing is grain size of the material, with larger grained material often hosting larger fractures when comparing between two otherwise identical materials (Eberhardt et al., 1999). The similarity between the two subunits would suggest a similar average grain-size between the two subunits, potentially favouring that the olivine present is a fine-grained fayalite if the clay-percentage within the subunits is high.

If the fracturing occurred due to desiccation, the presence of a higher percentage of clay in one subunit would have allowed larger fractures to form due to the increased capacity of the material to swell (Wilding et al., 1998; Hutchison, 2008). Conversely, if the mechanism is hydraulic fracturing, decreased percentages of clay in one of the subunits and the potential associated increase in the brittle nature of that subunit could have led to larger fractures forming (Guo et al., 2013). The very similar fracture metric distributions would consequently suggest a similar percentage of clay present in the two subunits.

Assuming that the fracture formation mechanism did not induce fracturing that could pass from one layer to another, differing polygon area sizes between the two subunits would have suggested differences in layer thickness, with thicker layers being found to have commensurately more widely spaced fractures in comparison to thinner layers (Schöpfer et al., 2011). The fact that polygon area was, for the most part, very similar between the different fracture sites looked at suggests that there is not a significant difference in layer thickness between the two subunits.

However why the "Blue Subunit 1" site has significantly larger fracture lengths and polygon areas is unknown. This could indicate, for the reasons outlined in the previous paragraphs, a variation in the properties of the Blue Subunit in this area and could consequently indicate more significant variation across the Blue Subunit than the other sites looked at would suggest. It could also indicate that the fracturing here originated via a different mechanism to that seen elsewhere in the Clay-bearing Unit. Further investigation will be required to constrain potential causes for this variation, and whether it is unique to the Blue Subunit in this area of Oxia Planum or is representative of wider variation across the site.

5. Conclusion

Within this paper we have shown a new, high resolution map of the Clay-bearing Unit at Oxia Planum, this map distinguishing between two subunits making up the wider Clay-bearing Unit as well including a third category for those exposures of the Clay-bearing Unit where it was difficult to discern which subunit it belonged to. This mapping was undertaken over the $1\sigma+$ landing envelope of the Rosalind Franklin rover where CaSSIS coverage was available, with this being an area of ~163 km^2 out of the ~181 km^2 covered by the envelope. From this mapping it was found that:

- ~18% of the $1\sigma+$ envelope is covered by exposures of the Orange Subunit, ~9% by exposures of the Blue Subunit, and ~12% by Indeterminate clay exposures.
- The south-east of the $1\sigma+$ landing envelope is dominated by exposures of the Orange Subunit, while the north-west has a more equal split between the Orange and Blue Subunits.

In addition to this clay map qualitative observations of the fracturing present within the Orange and Blue clay-bearing subunits were made,

with the fracture networks of a small number of these clay exposures also being mapped at a 50×50 m scale. It was found that:

- The fracture length distribution is broadly similar between the Blue Subunit in comparison to the Orange Subunit, in contrast with what has been reported previously.
- The polygon area distribution was also broadly similar between the two subunits, though the Blue Subunit polygon area distributions generally peaked at larger polygon sizes and extended to higher values than the Orange Subunit exposures.

These findings contrast with previous observations that the Blue Subunit displayed exclusively, or at least primarily, decametre-scale fracturing (Mandon et al., 2021). Consequently the presence of metre-scale fracturing within the clay exposures at Oxia Planum should not be used to preclude identification of a given exposure as belonging to the Blue Subunit. From the observed relation of the two subunits to each other, to the site's Dark Resistant Unit and to channels present within the mapped area, our favoured interpretation for the differences between the two subunits is constituent mineralogical differences, rather than differences in dust coverage, with this conclusion matching what was put forward in Mandon et al. (2021). Whether the Clay-bearing Unit is authigenic, with the differences between the subunits due to diagenesis or pedogenesis, or detrital, with variation in sediment coming into the site being responsible for the differences between the two subunits, is still unclear from orbital data alone. Ultimately investigations by the Rosalind Franklin Rover will be required to further clarify this issue.

Data availability

The CaSSIS images used in this study are available from the European Space Agency (ESA) at https://archives.esac.esa.int/psa/, while the HiRISE images used can be found on the University of Arizona's HiWish website; https://www.uahirise.org/hiwish/.

Author statement

Adam Parkes Bowen: Conceptualization, Methodology, Formal Analysis, Investigation, Writing - Original Draft, Writing - Review & Editing.

John Bridges: Conceptualization, Writing - Original Draft, Writing - Review & Editing, Supervision.

Livio Tornabene: Methodology, Resources, Writing - Original Draft, Writing - Review & Editing.

Lucia Mandon: Writing - Original Draft, Writing - Review & Editing.

Cathy Quantin-Nataf: Writing - Review & Editing.

Manish R. Patel: Writing - Review & Editing.

Nicolas Thomas: Writing - Review & Editing.

Gabriele Cremonese: Writing - Review & Editing.

Giovanni Munaretto: Writing - Review & Editing.

Antoine Pommerol: Writing - Review & Editing.

Maurizio Pajola: Writing - Review & Editing.

Declaration of competing interest

The authors declare that they have no known competing financial interests or personal relationships that could have appeared to influence the work reported in this paper.

References

Almeida, M., Read, M., Thomas, N., Cremonese, G., Becerra, P., Borrini, G., Byrne, S., Gruber, M., Heyd, R., Marriner, C. M., McArthur, G., McEwen, A. S., Pommerol, A., Perry, J. and Schaller, C. "Targeted planning of martian surface features with ExoMars/CaSSIS." Planetary and Space Science (Under Review).

Bibring, J.-P., Soufflot, A., Berthé, M., Langevin, Y., Gondet, B., Drossart, P., Bouyé, M., Combes, M., Puget, P., Semery, A., Bellucci, G., Formisano, V., Moroz, V., Kottsov, V., Bonello, G., Erard, S., Forni, O., Gendrin, A., Manaud, N., Poulet, F., Poulleau, G., Encrenaz, T., Fouchet, T., Melchiori, R., Altieri, F., Ignatiev, N., Titov, D., Zasova, L., Coradini, A., Capacionni, F., Cerroni, P., Fonti, S., Mangold, N., Pinet, P., Schmitt, B., Sotin, C., Hauber, E., Hoffmann, H., R, J., Keller, U., Arvidson, R., Mustard, J., Forget, F., 2004. OMEGA: Observatoire pour la Minéralogie, l'Eau, les Glaces et l'Activité. Mars Express: the scientific payload. ESA Publication Division, pp. 37–49.

Bridges, J.C., Schwenzer, S.P., Leveille, R., Westall, F., Wiens, R.C., Mangold, N., Bristow, T., Edwards, P., Berger, G., 2015. Diagenesis and clay mineral formation at Gale crater, mars. J Geophys Res Planets 120 (1), 1–19. https://doi.org/10.1002/2014JE004757.

Bristow, T.F., Grotzinger, J.P., Rampe, E.B., Cuadros, J., Chipera, S.J., Downs, G.W., Fedo, C.M., Frydenvang, J., McAdam, A.C., Morris, R.V., Achilles, C.N., Blake, D.F., Castle, N., Craig, P., Marais, D.J.D., Downs, R.T., Hazen, R.M., Ming, D.W., Morrison, S.M., Thorpe, M.T., Treiman, A.H., Tu, V., Vaniman, D.T., Yen, A.S., Gellert, R., Mahaffy, P.R., Wiens, R.C., Bryk, A.B., Bennett, K.A., Fox, V.K., Millken, R.E., Fraeman, A.A., Vasavada, A.R., 2021. Brine-driven destruction of clay minerals in Gale crater, Mars. Science 373 (6551), 198–204. https://doi.org/10.1126/science.abg5449.

Bush, A.L., 2001. In: Buschow, K.H.J., Cahn, R.W., Flemings, M.C., et al. (Eds.), Construction Materials Lightweight Aggregates. Encyclopedia of Materials: Science and Technology, pp. 1550–1558.

Calef III, F.J., Gengl, H.E., Soliman, T., Abercrombie, S.P., Powell, M.W., 2017. MMGIS A multi-mission geographic information system for insitu mars operations. In: 48th Lunar and Planetary Science Conference. The Woodlands Waterway Marriott Hotel & Convention Center, The Woodlands, Texas, United States.

Calef III, F.J., Soliman, T., Abarca, H.E., 2020. Multi-mission geographic information system:updates and mars science operations status. In: 51st Lunar and Planetary Science Conference. The Woodlands Waterway Marriott Hotel & Convention Center, The Woodlands, Texas, United States.

Carter, J., Quantin, C., Thollot, P., Loizeau, D., Ody, A., Lozach, a.L., 2016. Oxia Planum, A Clay-Laden Landing Site Proposed for the ExoMars Rover Mission: Acqueous Mineralogy and Alteration Scenarios. 47th Lunar and Planetary Science Conference. The Woodlands Waterway Marriott Hotel & Convention Center, The Woodlands, Texas, United States.

Caswell, T.E., Milliken, R.E., 2017. Evidence for hydraulic fracturing at Gale crater, Mars: implications for burial depth of the Yellowknife Bay formation. Earth Planet Sci. Lett. 468, 72–84. https://doi.org/10.1016/j.epsl.2017.03.033.

Chavez, P.S., 1988. An improved dark-object subtraction technique for atmospheric scattering correction of multispectral data. Remote Sens. Environ. 24 (3), 459–479. https://doi.org/10.1016/0034-4257(88)90019-3.

Chojnacki, M., Moersch, J., Wray, J.J., 2011. HIRISE analysis of the western rim of endeavour crater, Meridiani Planum, mars: morphology, composition and topography. In: 42nd Lunar and Planetary Science Conference, pp. 2272–2273. The Woodlands, Texas.

Daubar, I.J., Dundas, C.M., Byrne, S., Geissler, P., Bart, G.D., McEwen, A.S., Russell, P.S., Chojnacki, M., Golombek, M.P., 2016. Changes in blast zone albedo patterns around new martian impact craters. Icarus 267, 86–105. https://doi.org/10.1016/j.icarus.2015.11.032.

Delvigne, J., Bisdom, E., Sleeman, J.R., Stoops, G., 1979. Olivines, their pseudomorphs and secondary products. Pedologie 29 (3), 247–309. 102.100.100/297505.

Eberhardt, E., Stimpson, B., Stead, D., 1999. Effects of grain size on the initiation and propagation thresholds of stress-induced brittle fractures. Rock Mech. Rock Eng. 32 (2), 81–99. https://doi.org/10.1007/s006030050026.

Fawdon, P., Balme, M.R., Bridges, J., Davis, J.M., Gupta, S., Quantan-Nataf, a.C., 2019. The ancient fluvial catchment of Oxia Planum: the exomars 2020 rover landing site. In: 50th Lunar and Planetary Science Conference 2019. The Woodlands Waterway Marriott Hotel & Convention Center, The Woodlands, Texas, United States.

Fergason, R., 2014. Mars THEMIS Day IR Controlled Mosaic Oxia Palus 00N 315E 100 Mpp. U. A. S. Center. USGS Astrogeology Science Center. https://astrogeology.usgs .gov/search/map/Mars/Odyssey/THEMIS-Day-IR-Controlled-Mosaic/Mars-THEMIS -Day-IR-Controlled-Mosaic-Oxia-Palus-00N-315E-100mpp.

Fernando, J., Schmidt, F., Douté, S., 2016. Martian surface microtexture from orbital CRISM multi-angular observations A new perspective for the characterization of the geological processes. Planet. Space Sci. 128, 30–51. https://doi.org/10.1016/j.pss.2016.05.005.

Gary-Bicas, C.E., Rogers, A.D., 2021. Geologic and thermal characterization of Oxia Planum using mars odyssey THEMIS data. J. Geophys. Res.: Planets 126 (2). https://doi.org/10.1029/2020je006678.

Geospatial, L.H., 2021. Stretch types background. from. https://www.l3harrisgeospatial.com/docs/BackgroundStretchTypes.html, 2021.

Grotzinger, J.P., Sumner, D.Y., Kah, L.C., Stack, K., Gupta, S., Edgar, L., Rubin, D., Lewis, K., Schieber, J., Mangold, N., Milliken, R., Conrad, P.G., DesMarais, D., Farmer, J., Siebach, K., Calef III, F., Hurowitz, J., McLennan, S.M., Ming, D., Vaniman, D., Crisp, J., Vasavada, A., Edgett, K.S., Malin, M., Blake, D., Gellert, R., Mahaffy, P., Wiens, R.C., Maurice, S., Grant, J.A., Wilson, S., Anderson, R.C., Beegle, L., Arvidson, R., Hallet, B., Sletten, R.S., Rice, M., Bell III, J., Griffes, J., Ehlmann, B., Anderson, R.B., Bristow, T.F., Dietrich, W.E., Dromart, G., Eigenbrode, J., Fraeman, A., Hardgrove, C., Herkenhoff, K., Jandura, L., Kocurek, G., Lee, S., Leshin, L.A., Leveille, R., Limonadi, D., Maki, J., McCloskey, S., Meyer, M., Minitti, M., Newsom, H., Oehler, D., Okon, A., Palucis, M., Parker, T., Rowland, S., Schmidt, M., Squyres, S., Steele, A., Stolper, E., Summons, R., Treiman, A., Williams, R., Yingst, A., Team, M.S., 2014. A habitable fluvio-lacustrine environment at Yellowknife Bay, Gale crater, mars. Science 343 (6169). https://doi.org/10.1126/science.1242777, 1242777:1242771-1242714.

Guo, Z., Li, X.-Y., Liu, C., Feng, X., Shen, Y., 2013. A shale rock physics model for analysis of brittleness index, mineralogy, and porosity in the Barnett Shale. J. Geophys. Eng. 10 (2). https://doi.org/10.1088/1742-2132/10/2/025006.

Gwinner, K., Jaumann, R., Hauber, E., Hoffmann, H., Heipke, C., Oberst, J., Neukum, G., Ansan, V., Bostelmann, J., Dumke, A., Elgner, S., Erkeling, G., Fueten, F., Hiesinger, H., Hoekzema, N.M., Kersten, E., Loizeau, D., Matz, K.D., McGuire, P.C., Mertens, V., Michael, G., Pasewaldt, A., Pinet, P., Preusker, F., Reiss, D., Roatsch, T., Schmidt, R., Scholten, F., Spiegel, M., Stesky, R., Tirsch, D., van Gasselt, S., Walter, S., Wählisch, M., Willner, K., 2016. The high resolution stereo camera (HRSC) of mars express and its approach to science analysis and mapping for mars and its satellites. Planet. Space Sci. 126, 93–138. https://doi.org/10.1016/j.pss.2016.02.014.

Hashim, R., Muntohar, A.S., 2006. Swelling rate of expansive clay soils. In: Al-Rawas, A.A., Goosen, M.F.A. (Eds.), Expansive Soils: Recent Advances in Characterization and Treatment, 1st ed. Taylor and Francis Group, pp. 139–148.

Holmes, J.A., Lewis, S.R., Patel, M.R., 2020. OpenMARS A global record of martian weather from 1999 to 2015. Planet. Space Sci. 188. https://doi.org/10.1016/j.pss.2020.104962.

Huang, J., Chu, X., Lyons, T.W., Planavsky, N.J., Wen, H., 2013. A new look at saponite formation and its implications for early animal records in the Ediacaran of South China. Geobiology 11 (1), 3–14. https://doi.org/10.1111/gbi.12018.

Hutchison, K., 2008. Characterization of Soil Shrink-Swell Potential Using the Texas VNIR Diffuse Reflectance Spectroscopy, vol. 39. Library, Texas A&M.

Léveillé, R.J., Bridges, J., Wiens, R.C., Mangold, N., Cousin, A., Lanza, N., Forni, O., Ollila, A., Grotzinger, J., Clegg, S., Siebach, K., Berger, G., Clark, B., Fabre, C., Anderson, R., Gasnault, O., Blaney, D., Deflores, L., Leshin, L., Maurice, S., Newsom, H., 2014. Chemistry of fracture-filling raised ridges in Yellowknife Bay, Gale Crater: window into past aqueous activity and habitability on Mars. J. Geophys. Res.: Planets 119 (11), 2398–2415. https://doi.org/10.1002/2014je004620.

Levy, J.S., Head, J.W., Marchant, D.R., 2008. The role of thermal contraction crack polygons in cold-desert fluvial systems. Antarct. Sci. 20 (6), 565–579. https://doi.org/10.1017/S0954102008001375.

Levy, J.S., Head, J.W., Marchant, D.R., 2009. Thermal contraction crack polygons on Mars: classification, distribution, and climate implications from HiRISE observations. J. Geophys. Res. 114 (E1). https://doi.org/10.1029/2008je003273.

Maechler, M., Team, R., 2021a. Bandwidth selectors for kernel density estimation. R manual. Retrieved 02/02/2021, 2021, from. https://stat.ethz.ch/R-manual/R-devel/library/stats/html/density.html.

Maechler, M., Team, R., 2021b. Kernel density estimation. R manual. Retrieved 02/02/2021, 2021, from. https://stat.ethz.ch/R-manual/R-devel/library/stats/html/density.html.

Mandon, L., Parkes-Bowen, A., Quantin-Nataf, C., Bridges, J.C., Carter, J., Pan, L., Beck, P., Dehouck, E., Volat, M., Thomas, N., Cremonese, G., Tornabene, L.L., 2021. Morphological and spectral diversity of the clay-bearing unit at the ExoMars landing site Oxia Planum. Astrobiology 21 (4), 464–480. https://doi.org/10.1089/ast.2020.2292.

Mastropietro, M., Pajola, M., Cremonese, G., Munaretto, G., Lucchetti, A., 2020. Boulder analysis on the Oxia Planum ExoMars 2022 rover landing site: scientific and engineering perspectives. Sol. Syst. Res. 54, 504–519. https://doi.org/10.1134/S0038094620060040.

McEwen, A.S., Eliason, E.M., Bergstrom, J.W., Bridges, N.T., Hansen, C.J., Delamere, W.A., Grant, J.A., Gulick, V.C., Herkenhoff, K.E., Keszthelyi, L., Kirk, R.L., Mellon, M.T., Squyres, S.W., Thomas, N., Weitz, a.C.M., 2007. Mars reconnaissance orbiter's high resolution imaging science experiment (HiRISE). J. Geophys. Res.: Planets 112 (E5). https://doi.org/10.1029/2005JE002605.

Milazzo, M.P., Herkenhoff, K., Becker, K., Russell, P., Delamere, A., McEwen, A.S., 2015. MRO/HiRISE radiometric calibration update. In: 46th Lunar and Planetary Science Conference.

Molina, A., López, I., Prieto-Ballesteros, O., Fernández-Remolar, D., Pablo, M.Á., Gómez, F., 2017. Coogoon Valles, western Arabia Terra: hydrological evolution of a complex martian channel system. Icarus 293, 27–44. https://doi.org/10.1016/j.icarus.2017.04.002.

Munaretto, G., Pajola, M., Cremonese, G., Re, C., Lucchetti, A., Simioni, E., McEwen, A.S., Pommerol, A., Becerra, P., Conway, S.J., Thomas, N., Massironi, M., 2020. Implications for the origin and evolution of martian recurring slope lineae at hale crater from CaSSIS observations. Planet. Space Sci. 187. https://doi.org/10.1016/j.pss.2020.104947.

Murchie, S., Arvidson, R., Bedini, P., Beisser, K., Bibring, J.-P., Bishop, J., Boldt, J., Cavender, P., Choo, T., Clancy, R.T., Darlington, E.H., Marais, D.D., Espiritu, R., Fort, D., Green, R., Guinness, E., Hayes, J., Hash, C., Heffernan, K., Hemmler, J., Heyler, G., Humm, D., Hutcheson, J., Izenberg, N., Lee, R., Lees, J., Lohr, D., Malaret, E., Martin, T., McGovern, J.A., McGuire, P., Morris, R., Mustard, J., Pelkey, S., Rhodes, E., Robinson, M., Roush, T., Schaefer, E., Seagrave, G., Seelos, F., Silverglate, P., Slavney, S., Smith, M., Shyong, W.-J., Strohbehn, K., Taylor, H., Thompson, P., Tossman, B., Wirzburger, M., Wolff, M., 2007. Compact reconnaissance imaging spectrometer for mars (CRISM) on mars reconnaissance orbiter (MRO). J. Geophys. Res.: Planets 112 (E5), 57. https://doi.org/10.1029/2006JE002682.

Olphen, H.v., 1965. Thermodynamics of interlayer adsorption of water in clays. J. Colloid Sci. 20 (8), 822–837. https://doi.org/10.1016/0095-8522(65)90055-3.

Olsen, A.A., Rimstidt, J.D., 2007. Using a mineral lifetime diagram to evaluate the persistence of olivine on Mars. Am. Mineral. 92 (4), 598–602. https://doi.org/10.2138/am.2007.2462.

Pajola, M., Rossato, S., Baratti, E., Pozzobon, R., Quantin, C., Carter, J., Thollot, P., 2017. Boulder abundances and size-frequency distributions on Oxia Planum-Mars: scientific implications for the 2020 ESA ExoMars rover. Icarus 296, 73–90. https://doi.org/10.1016/j.icarus.2017.05.011.

Parzen, E., 1962. On estimation of a probability density function and mode. Ann. Math. Stat. 33 (3), 1065–1076. https://doi.org/10.1214/aoms/1177704472.

Perry, J. E., Heyd, R., Read, M., Tornabene, L. L., Sutton, S., Byrne, S., Thomas, N., Fennema, A., McEwen, A. and Berry, K. "Geometric processing of TGO CaSSIS observations." Planetary and Space Science (Under Review).

Plummer, P.S., Gostin, V.A., 1981. Shrinkage cracks desiccation or synaeresis. J. Sediment. Petrol. 51 (4), 1147–1156. https://doi.org/10.1306/212F7E4B-2B24-11D7-8648000102C1865D.

Pommerol, A., Thomas, N., Almeida, M., Read, M., Becerra, P., Cesar, C., Valantinas, A., Simioni, E., McEwen, A. S., Perry, J., Marriner, C., Munaretto, G., Pajola, M., Tornabene, L., Mege, D., Deppo, V. D., Re, C. and Cremonese, G. (this issue). "In-flight radiometric calibration of the ExoMars TGO colour and stereo surface imaging system." Planetary and Space Science (Under Review).

Quantin-Nataf, C., Carter, J., Mandon, L., Thollot, P., Balme, M., Volat, M., Pan, L., Loizeau, D., Millot, C., Breton, S., Dehouck, E., Fawdon, P., Gupta, S., Davis, J., Gringrod, P., Pacifici, A., Bultel, B., Allemand, P., Ody, A., Lozach, L., Broyer, J., 2021. Oxia Planum - the landing site for the ExoMars "Rosalind Franklin" rover mission: geological context and pre-landing interpretation. Astrobiology 21 (3), 345–366. https://doi.org/10.1089/ast.2019.2191.

Quantin-Nataf, C., Carter, J., Thollot, P., Broyer, J., Lozach, L., Davis, J., Grindrod, P., Pajola, M., Baratti, E., Rossato, S., Allemand, P., Bultel, B., Leyrat, C., Fernando, J., Ody, A., 2015. Oxia Planum a Suitable Landing Site for ExoMars 2018 Rover, vol. 10. EPSC. La Cité des Congrès, Nantes, France.

Quantin-Nataf, C., Carter, J., Thollot, P., Broyer, J., Lozach, L., Fawdon, P., Davis, J., Grindrod, P., Balme, M., Fernando, J., Pajola, N., Baratti, E., Sandro, R., Allemand, P., Bultel, B., Leyrat, C., Ody, A., 2017. Oxia Planum LSSW4 Site Report. Fifth Landing Site Selection Working Group, Unpublished.

Rampe, E.B., Blake, D.F., Bristow, T.F., Ming, D.W., Vaniman, D.T., Morris, R.V., Achilles, C.N., Chipera, S.J., Morrison, S.M., Tu, V.M., Yen, A.S., Castle, N., Downs, G.W., Downs, R.T., Grotzinger, J.P., Hazen, R.M., Treiman, A.H., Peretyazhko, T.S., Des Marais, D.J., Walroth, R.C., Craig, P.I., Crisp, J.A., Lafuente, B., Morookian, J.M., Sarrazin, P.C., Thorpe, M.T., Bridges, J.C., Edgar, L.A., Fedo, C.M., Freissinet, C., Gellert, R., Mahaffy, P.R., Newsom, H.E., Johnson, J.R., Kah, L.C., Siebach, K.L., Schieber, J., Sun, V.Z., Vasavada, A.R., Wellington, D., Wiens, R.C., 2020. Mineralogy and geochemistry of sedimentary rocks and eolian sediments in Gale crater, Mars: a review after six Earth years of exploration with Curiosity. Geochemistry 80 (2). https://doi.org/10.1016/j.chemer.2020.125605.

Roloff, V., Pommerol, A., Gambicorti, L., Servonet, A., Thomas, N., Brändli, M., Casciello, A., Cremonese, G., Deppo, V.D., Erismann, M., Veltroni, I.F., Gerber, M., Gruber, M., Gubler, P., Hausner, T., Johnson, M., Lochmatter, P., Pelò, E., Sodor, B., Szalai, S., Troznai, G., Vernani, D., Weigel, T., Zieth, R., Zimmermann, C., 2017. On-ground performance and calibration of the ExoMars trace Gas orbiter CaSSIS imager. Space Sci. Rev. 212, 1871–1896. https://doi.org/10.1007/s11214-017-0404-2.

Rosenblatt, M., 1956. Remarks on some nonparametric estimates of a density function. Ann. Math. Stat. 27 (3), 832–837. https://doi.org/10.1214/aoms/1177728190.

RRUFF-Project, 2001a. Saponite. Version 1.2. Retrieved 13/11/21, 2021, from. https://rruff.info/doclib/hom/saponite.pdf.

RRUFF-Project, 2001b. Vermiculite. Version 1.2. Retrieved 13/11/21, 2021, from. https://rruff.info/doclib/hom/vermiculite.pdf.

Ruff, S.W., Christensen, P.R., 2002. Bright and dark regions on Mars: particle size and mineralogical characteristics based on thermal emission spectrometer data. J. Geophys. Res.: Planets 107 (E12). https://doi.org/10.1029/2001JE001580.

Sacks, L.E., Tornabene, L.L., Osinski, G.R., McEwen, A.S., Sopoco, R.M., 2020. HiRISE Band Ratios and CRISM Spectral Results at Hargraves Crater. 51st Lunar and Planetary Science Conference.

Scherer, G.W., 1989. Mechanics of synersis I. Theory. J. Non-Cryst. Solids 108 (1), 18–27. https://doi.org/10.1016/0022-3093(89)90328-1.

Schöpfer, M.P.J., Arslan, A., Walsh, J.J., Childs, C., 2011. Reconciliation of contrasting theories for fracture spacing in layered rocks. J. Struct. Geol. 33 (4), 551–565. https://doi.org/10.1016/j.jsg.2011.01.008.

Sefton-Nash, E., Balme, M., Quantin-Nataf, C., Fawdon, P., Volat, M., Hauber, E., Orgel, C., Frigeri, A., Le Deit, L., Ruesch, O., Adeli, S., Loizeau, D., Davis, J., Grindrod, P., Nass, A., de Witte, S., Calef, F.J., Soliman, T.K., Vago, J.L., 2020. HiRISE-scale characterization of the Oxia Planum landing site for the Exomars 2022 mission. Europlanet Sci. Congr. 14, 1–4. https://doi.org/10.5194/epsc2020-978, 978 held virtually.

Sheather, S.J., Jones, M.C., 1991. A reliable data-based bandwidth selection method for kernel density estimation. J. Roy. Stat. Soc. B 53 (3), 683–690. https://doi.org/10.2307/2345597.

Silvestro, S., Pacifici, A., Salese, F., Vaz, D.A., Neesemann, A., Tirsch, D., Popa, C.I., Pajola, M., Franzese, G., Mongelluzzo, G., Ruggeri, A.C., Cozzolino, F., Porto, C., Esposito, F., 2021. Periodic Bedrock ridges at the ExoMars 2022 landing site: evidence for a changing wind regime. Geophys. Res. Lett. 48 (4). https://doi.org/10.1029/2020GL091651.

Smith, M.D., 2008. Spacecraft observations of the martian atmosphere. Annu. Rev. Earth Planet Sci. 36 (1), 191–219. https://doi.org/10.1146/annurev.earth.36.031207.124334.

Stopar, J.D., Jeffrey Taylor, G., Hamilton, V.E., Browning, L., 2006. Kinetic model of olivine dissolution and extent of aqueous alteration on mars. Geochem. Cosmochim. Acta 70 (24), 6136–6152. https://doi.org/10.1016/j.gca.2006.07.039.

Suquet, H., Iiyama, J.T., Kodamat, H., Pezerat, H., 1977. Synthesis and swelling properties of saponites with increasing layer charge. Clay Clay Miner. 25, 231–242. https://doi.org/10.1346/CCMN.1977.0250310.

Tanaka, K.L., Skinner, J.A., Dohm, J.M., I III, R.P., Kolb, E.J., Fortezzo, C.M., Platz, T., Michael, G.G., Hare, T.M., 2014. Geologic Map of Mars. Scientific Investigations Map, National Aeronautics and Space Administration.

Thomas, N., Cremonese, G., Ziethe, R., Gerber, M., Brändli, M., Bruno, G., Erismann, M., Gambicorti, L., Gerber, J., Ghose, K., Gruber, M., Gubler, P., Mischler, H., Jost, J., Piazza, D., Pommerol, A., Rieder, M., Roloff, V., Servonet, A., Trottmann, W., Uthaicharoenpong, T., Zimmermann, C., Vernani, D., Johnson, M., Pelò, E., Weigel, T., Viertl, J., Roux, N.D., Lochmatter, P., Sutter, G., Casciello, A., Hausner, T., Veltroni, I.F., Deppo, V.D., Orleanski, P., Nowosielski, W., Zawistowski, T., Szalai, S., Sodor, B., Tulyakov, S., Troznai, G., Banaskiewicz, M., Bridges, J.C., Byrne, S., Debei, S., El-Maarry, M.R., Hauber, E., Hansen, C.J., Ivanov, A., Keszthelyi, L., Kirk, R., Kuzmin, R., Mangold, N., Marinangeli, L., Markiewicz, W.J., Massironi, M., McEwen, A.S., Okubo, C., Tornabene, L.L., Wajer, P., Wray, J.J., 2017. The colour and stereo surface imaging system (CaSSIS) for the ExoMars trace Gas orbiter. Space Sci. Rev. 212 (3–4), 1897–1944. https://doi.org/10.1007/s11214-017-0421-1.

Thomas, N., Pommerol, A., Almeida, M., Read, M., Cremonese, G., Simioni, E., Munaretto, G. and Weigel, T. "Absolute calibration of the colour and stereo surface imaging system (CaSSIS)." Planetary and Space Science this issue 211, https://doi.org/10.1016/j.pss.2021.105394.

Tornabene, L.L., Osinski, G.R., McEwen, A.S., Wray, J.J., Craig, M.A., Sapers, H.M., Christensen, P.R., 2013. An impact origin for hydrated silicates on Mars: a synthesis. J. Geophys. Res.: Planets 118 (5), 994–1012. https://doi.org/10.1002/jgre.20082.

Tornabene, L.L., Seelos, F.P., Pommerol, A., Thomas, N., Caudill, C.M., Becerra, P., Bridges, J.C., Byrne, S., Cardinale, M., Chojnacki, M., Conway, S.J., Cremonese, G., Dundas, C.M., El-Maarry, M.R., Fernando, J., Hansen, C.J., Hansen, K., Harrison, T.N., Henson, R., Marinangeli, L., McEwen, A.S., Pajola, M., Sutton, S.S., Wray, J.J., 2018. Image simulation and assessment of the colour and spatial capabilities of the colour and stereo surface imaging system (CaSSIS) on the ExoMars trace Gas orbiter. Space Sci. Rev. 214 (1). https://doi.org/10.1007/s11214-017-0436-7.

Tornabene, L. L., Thomas, N. and Cremonese, G. (in prep). "CaSSIS Colour and Multispectral Analysis." in prep. *doi*: n/a.

Vago, J.L., Westall, F., Coates, A.J., Jaumann, R., Korablev, O., Ciarletti, V., Mitrofanov, I., Josset, J.L., De Sanctis, M.C., Bibring, J.P., Rull, F., Goesmann, F., Steininger, H., Goetz, W., Brinckerhoff, W., Szopa, C., Raulin, F., Westall, F., Edwards, H.G.M., Whyte, L.G., Fairen, A.G., Bibring, J.P., Bridges, J., Hauber, E., Ori, G.G., Werner, S., Loizeau, D., Kuzmin, R.O., Williams, R.M.E., Flahaut, J., Forget, F., Vago, J.L., Rodionov, D., Korablev, O., Svedhem, H., Sefton-Nash, E., Kminek, G., Lorenzoni, L., Joudrier, L., Mikhailov, V., Zashchirinskiy, A., Alexashkin, S., Calantropio, F., Merlo, A., Poulakis, P., Witasse, O., Bayle, O., Bayon, S., Meierhenrich, U., Carter, J., Garcia-Ruiz, J.M., Baglioni, P., Haldemann, A., Ball, A.J., Debus, A., Lindner, R., Haessig, F., Monteiro, D., Trautner, R., Voland, C., Rebeyre, P., Goulty, D., Didot, F., Durrant, S., Zekri, E., Koschny, D., Toni, A., Visentin, G., Zwick, M., van Winnendael, M., Azkarate, M., Carreau, C., 2017. Habitability on early mars and the search for biosignatures with the ExoMars rover. Astrobiology 17 (6–7), 471–510. https://doi.org/10.1089/ast.2016.1533.

Vago, J.L., Witasse, O., Svedhem, H., Baglioni, P., Haldemann, A., Gianfiglio, G., Blancquaert, T., McCoy, D., Groot, R.d., 2015. ESA ExoMars program: the next step in exploring Mars. Sol. Syst. Res. 49 (7), 518–528. https://doi.org/10.1134/s0038094615070199.

van der Meer, F.D., van der Werff, H.M.A., van Ruitenbeek, F.J.A., Hecker, C.A., Bakker, W.H., Noomen, M.F., van der Meijde, M., Carranza, E.J.M., Smeth, J.B.d., Woldai, T., 2012. Multi- and hyperspectral geologic remote sensing: a review. Int. J. Appl. Earth Obs. Geoinf. 14 (1), 112–128. https://doi.org/10.1016/j.jag.2011.08.002.

Vaniman, D.T., Bish, D.L., Ming, D.W., Bristow, T.F., Morris, R.V., Blake, D.F., Chipera, S.J., Morrison, S.M., Treiman, A.H., Rampe, E.B., Rice, M., Achilles, C.N., Grotzinger, J.P., McLennan, S.M., Williams, J., B III, J.F., Newsom, H.E., Downs, R.T., Maurice, S., Sarrazin, P., Yen, A.S., Morookian, J.M., Farmer, J.D., Stack, K., Milliken, R.E., Ehlmann, B.L., Sumner, D.Y., Berger, G., Crisp, J.A., Hurowitz, J.A., Anderson, R., Marais, D.J.D., Stolper, E.M., Edgett, K.S., Gupta, S., Spanovich, N., Team, M.S., 2014. Mineralogy of a Mudstone at Yellowknife Bay, Gale crater, mars. Science 343 (6169). https://doi.org/10.1126/science.1243480.

Velde, B., Meunier, A., 2008. The Origin of Clay Minerals in Soils and Weathered Rocks. Springer, Berlin, Heidelberg. Springer.

Viviano-Beck, C.E., Seelos, F.P., Murchie, S.L., Kahn, E.G., Seelos, K.D., Taylor, H.W., Taylor, K., Ehlmann, B.L., Wiseman, S.M., Mustard, J.F., Morgan, M.F., 2014. Revised CRISM spectral parameters and summary products based on the currently detected mineral diversity on Mars. J. Geophys. Res.: Planets 119 (6), 1403–1431. https://doi.org/10.1002/2014je004627.

Weaver, C.E., 1973. In: Weaver, C.E., Pollard, L.D. (Eds.), Vermiculite. The Chemistry of Clay Minerals, vol. 15, pp. 99–106.

Westall, F., Edwards, H.G., Whyte, L., Fairén, A.G., Bibring, J.-P., Bridges, J., Hauber, E., Ori, G.G., Werner, S., Loizeau, D., Kuzmin, R., Williams, R.M.E., Flahaut, J., Forget, F., Vago, J.L., Rodionov, D., Korablev, O., Witasse, O., Kminek, G., Lorenzoni, L., Bayle, O., Joudrier, L., Mikhailov, V., Zashirinsky, A., Alexashkin, S., Calantropio, F., Merlo, A., 2014. Recommendation for the Narrowing of ExoMars 2018 Landing Sites.

Wilding, L.P., Tessier, D., 1998. In: Wilding, L.P., Puentes, R. (Eds.), Genesis of Vertisols: Shrink-Swell Phenomena. Vertisols: Their Distribution, Properties, Classification, and Management, pp. 55–79.

Wogelius, R.A., Walther, J.V., 1991. Olivine dissolution at 25°C Effects of pH, CO_2, and organic acids. Geochem. Cosmochim. Acta 55 (4), 943–954. https://doi.org/10.1016/0016-7037(91)90153-V.

Wogelius, R.A., Walther, J.V., 1992. Olivine dissolution kinetics at near-surface conditions. Chem. Geol. 97 (1–2), 101–112. https://doi.org/10.1016/0009-2541(92)90138-U.

Wolff, M.J., Clancy, R.T., Kahre, M.A., Haberle, R.M., Forget, F., Cantor, B.A., Malin, M.C., 2019. Mapping water ice clouds on Mars with MRO/MARCI. Icarus 332, 24–49. https://doi.org/10.1016/j.icarus.2019.05.041.

Wolff, M.J., Smith, M.D., Clancy, R.T., Arvidson, R., Kahre, M., Seelos, F., Murchie, S., Savijärvi, H., 2009. Wavelength dependence of dust aerosol single scattering albedo as observed by the Compact Reconnaissance Imaging Spectrometer. J. Geophys. Res. 114 (E2). https://doi.org/10.1029/2009je003350.

Yang, W., Zheng, Y., Zaoui, A., 2015. Swelling and diffusion behaviour of Na-vermiculite at different hydrated states. Solid State Ionics 282, 13–17. https://doi.org/10.1016/j.ssi.2015.09.007.

Zeeb, C., Gomez-Rivas, E., Bons, P.D., Blum, P., 2013. Evaluation of sampling methods for fracture network characterization using outcrops. AAPG (Am. Assoc. Pet. Geol.) Bull. 97 (9), 1545–1566. https://doi.org/10.1306/02131312042.

Zielinski, W., Węglarczyk, S., Kuchar, L., Michalski, A., Kazmierczak, B., 2018. Kernel density estimation and its application. ITM Web Conf. 23 (2). https://doi.org/10.1051/itmconf/20182300037.